Research Square

Preprints are preliminary reports that have not undergone peer review.
They should not be considered conclusive, used to inform clinical practice,
or referenced by the media as validated information.

Scalable, unsupervised, and annotation-free discovery of cell–cell communication modules across 2D and 3D spatial omics with STARComm

Khoa Huynh
VCU Massey Comprehensive Cancer Center
Bruno Matuck
Hospital Israelita Albert Einstein
Deiziane Souza
Virginia Commonwealth University
XiuYu Zhang
Virginia Commonwealth University
Elizabeth Godschall
Virginia Commonwealth University
Giancarlo Fatobene
Universidade de São Paulo
Luiz Alberto Valente Soares Junior
Universidade de São Paulo
Luiz Fernando Ferraz da Silva
Universidade de São Paulo
Vanderson Geraldo Rocha
Universidade de São Paulo
Kevin Byrd
Virginia Commonwealth University
Jinze Liu
liuj15@vcu.edu

Virginia Commonwealth University

Research Article

Keywords: Spatial transcriptomics, Spatial omics, Cell–cell communication, Multicellular communication modules, Benchmarking, Three-dimensional spatial omics, Scalable methods, Tumor microenvironment, Chronic graft-versus-host disease

Posted Date: November 23rd, 2026

DOI: https://doi.org/10.21203/rs.3.rs-11434726/v1

License: This work is licensed under a Creative Commons Attribution 4.0 International License.
Read Full License

Additional Declarations:
Competing interest reported. The authors had access to the study data and reviewed and approved the final manuscript. Although the authors view each of these as noncompeting financial interests, KMB and BFM are active members of the Human Cell Atlas; Furthermore, K.M.B. is a scientific advisor at Arcato Laboratories (Durham, NC) as well as the CEO and co-founder of Stratica Biosciences (Durham, NC); JL is a CTO and co-founder of Stratica Biosciences. All other authors declare no competing interests.

Table 1 is available in the Supplementary Files section.

Scalable, unsupervised, and annotation-free discovery of cell–cell communication modules across 2D and 3D spatial omics with STARComm

Khoa L. A. Huynh[1, 8], Bruno F. Matuck[2], Deiziane de Souza[3], XiuYu Zhang[1], Elizabeth Godschall[3], Giancarlo Fatobene[5], Luiz Alberto Valente Soares Junior[6], Luiz Fernando Ferraz da Silva[4], Vanderson Geraldo Rocha[7], Kevin M. Byrd[3, 8#], Jinze Liu[1, 8#]

[1] Department of Biostatistics, Virginia Commonwealth University, Richmond, VA, USA.

[2] Hospital Israelita Albert Einstein, São Paulo, SP, Brazil

[3] Department of Oral and Craniofacial Molecular Biology, Philips Institute for Oral Health Research, Virginia Commonwealth University, Richmond, VA, USA.

[4] Department of Pathology, Medicine School of University of Sao Paulo, São Paulo, SP, Brazil.

[5] Laboratório de Investigação Médica (LIM), Hospital das Clínicas, Faculdade de Medicina, Universidade de São Paulo, São Paulo, SP, Brazil.

[6] Division of Dentistry of Hospital das Clinicas of University of Sao Paulo, São Paulo, SP, Brazil.

[7] Department of Hematology, Transfusion and Cell Therapy Service, University of São Paulo, São Paulo, SP, Brazil.

[8] Massey Comprehensive Cancer Center, Virginia Commonwealth University, Richmond, VA, USA

[#] CORRESPONDING AUTHORS:

Jinze Liu: liuj15@vcu.edu

Kevin Matthew Byrd: kevinmbyrd@gmail.com

KEYWORDS:

Spatial transcriptomics, Spatial omics, Cell–cell communication, Multicellular communication modules, Benchmarking, Three-dimensional spatial omics, Scalable methods, Tumor microenvironment, Chronic graft-versus-host disease

ABSTRACT

Background: Spatial transcriptomics enables cell–cell communication to be studied within intact tissue, but most spatially aware methods score individual ligand–receptor pairs, depend on prior cell-type annotation, scale poorly to large datasets, or do not support three-dimensional data. Methods that identify higher-order communication programs directly from spatial coordinates are lacking.

Results: We present STARComm, an unsupervised, annotation-free method that detects cell-level ligand–receptor proximity events, converts them into kernel density profiles, and clusters co-localized profiles into multicellular communication interaction modules (MCIMs). In simulations with known ground truth, STARComm recovered modules more accurately than COMMOT, SpatialDM, and an expression-only baseline, particularly under sparse and low-signal conditions (adjusted Rand index 0.70 versus 0.20, 0.01, and 0.01 at 10% communication density), and its modules were more spatially coherent. In tissue benchmarks, STARComm produced more spatially coherent modules than COMMOT and SpatialDM (Moran's I 0.91 versus 0.19 and 0.13 in a uterine cancer region) while reducing runtime from hours to minutes. We then demonstrated generalizability across platforms, scales, and dimensions: a 35-tissue Xenium cohort of chronic graft-versus-host disease salivary glands, a 16-region MERSCOPE pan-cancer dataset of more than 14.5 million cells, more than 2.5 million Visium HD bins, and a 362,704-cell three-dimensional mouse-brain volume with paired Deep-STARmap transcriptomic and Deep-RIBOmap translatomic layers, in which virtual two-dimensional sections retained approximately 7% of the communication events detected in three dimensions.

Conclusions: STARComm is a scalable method for identifying higher-order spatial communication programs in two- and three-dimensional spatial omics data. It is designed for

communication-module discovery rather than for every cell–cell communication task, and the modules it identifies provide hypotheses for downstream biological and therapeutic validation.

BACKGROUND

Tissues are composed of spatially organized and phenotypically diverse cell populations that coordinate their behavior through continuous molecular exchange. Among these mechanisms, ligand–receptor (L–R) interactions provide a major route for cell-cell communication (CCC), regulating processes such as proliferation, differentiation, immune activation, tissue repair, and pathological remodeling[1–3]. Single-cell RNA sequencing has enabled systematic inference of CCC from gene expression data, leading to widely used methods such as CellChat[4], NicheNet[5], CellPhoneDB[6], LIANA+[7], NATMI[8], and scSeqComm[9]. These approaches established an important computational paradigm for scoring potential L–R interactions between annotated cell populations. However, scRNA-seq alone does not preserve the spatial information needed to determine whether putative interacting cells are physically proximal. As a result, they may infer communication events between cell populations that are transcriptionally compatible but spatially separated, limiting their ability to resolve communication architecture within intact tissues[10,11].

Spatial transcriptomics technologies address this limitation by measuring gene expression within preserved tissue architecture, thereby enabling CCC inference in its native spatial context[11]. A second generation of computational methods has incorporated spatial information into L–R analysis using distance cutoffs, spatial graphs, diffusion models, or spatially aware regression. For example, CellChat v2[4] extends population-level communication analysis by incorporating spatial constraints and pattern discovery; SpaTalk[12] uses spatial cell-type graphs and pathway knowledge to infer signaling routes; stMLnet[13] models multilayer signal propagation from ligand to receptor to downstream transcriptional targets; SpaCCC[14] and related frameworks quantify spatially constrained communication events; and TWCOM[15] uses regression modeling to evaluate distance-dependent L–R associations (Table 1). These methods have substantially improved the biological plausibility of inferred communication events by accounting for spatial proximity. Nevertheless, many depend on cell-type annotations and summarize communication at the level of predefined cell populations. Their outputs are therefore constrained by the

granularity, accuracy and reproducibility of upstream clustering and annotation pipelines, and they may not capture communication activity within spatially localized cellular niches.

More recent annotation-free methods have further advanced the field by modeling CCC directly from spatial coordinates without requiring prior cell-type labels. COMMOT[10] uses collective optimal transport to infer directional communication flow; SpatialDM[11] applies bivariate spatial autocorrelation to identify spatially co-expressed L–R pairs; and CellNEST[16] uses graph attention and contrastive learning to model relay-like communication networks across spatial neighborhoods (Table 1). These approaches represent an important conceptual shift from population-level communication inference toward spatially resolved, cell-level analysis. However, their outputs remain centered on individual L–R pairs, local pairwise edges, directional signaling vectors or relay networks. Thus, they are not designed to directly answer a broader biological question: how multiple L–R interactions act together within the same tissue region to form higher-order multicellular communication programs.

This gap is increasingly important as modern spatial technologies generate datasets with hundreds of thousands to millions of cells, spatial bins, or spots. Imaging-based platforms such as Xenium and MERSCOPE can profile large numbers of spatially resolved cells, while sequencing-based approaches such as VisiumHD provide high-resolution spatial transcriptomic measurements across tissue sections[17,18]. Emerging three-dimensional methods further extend spatial profiling into volumetric tissue architecture. These technologies create new opportunities to study communication at tissue scale, but they also introduce computational challenges. High-plex spatial datasets often contain sparse measurements, extensive cellular heterogeneity, and large sample sizes. Existing methods may therefore struggle to detect statistically robust global co-localization patterns, scale efficiently to large datasets, or identify coordinated multi-pair communication programs rather than isolated L–R interactions.

To address these challenges, we introduce the concept of Multicellular Communication Interaction Modules (MCIMs). MCIMs are spatially coherent tissue neighborhoods in which

multiple L–R interactions are jointly enriched, representing higher-order communication hubs rather than individual pairwise signaling events. This concept is motivated by the observation that tissue functions and disease states are rarely driven by a single signaling axis. Instead, immune activation, stromal remodeling, angiogenesis, epithelial repair and tumor progression often emerge from coordinated signaling among multiple cell populations within a shared microenvironment. By modeling these co-localized signaling programs, MCIMs provide a framework for describing the multicellular communication architecture of tissues. MCIMs differ from cellular neighborhoods, which are defined by the local cell-type composition of a tissue region: MCIMs are defined by the co-localized density of ligand–receptor communication events and are identified without cell-type labels, so that regions with similar composition can belong to different MCIMs when their signaling differs.

We developed STARComm, a scalable, unsupervised, and annotation-free framework for identifying MCIMs from spatial transcriptomics data. STARComm combines data-driven identification of spatially proximal L–R events with spatial density estimation and clustering of co-localized signaling patterns. Because MCIM detection is performed directly from spatial coordinates and L–R expression, STARComm does not require cell-type annotations as input, although annotations can be incorporated downstream to interpret the cellular composition and biological functions of each module. This design enables STARComm to move beyond individual L–R pairs and resolve higher-order multicellular communication programs across both two-dimensional and three-dimensional spatial datasets.

In this study, we present STARComm as a new, scalable method for identifying higher-order spatial communication programs and evaluate it first as a method. We benchmarked STARComm against COMMOT, SpatialDM, and an expression-only baseline using simulations with known ground truth, assessing module recovery, spatial coherence, robustness to signal strength, communication density, number of ligand–receptor pairs and key parameters, and computational performance, and then compared methods on experimental tissue. We then

applied STARComm to four datasets—chronic graft-versus-host disease salivary glands (Xenium), a pan-cancer atlas (MERSCOPE), colorectal cancer (Visium HD), and a three-dimensional mouse-brain volume with paired transcriptomic and translatomic layers (Deep-STARmap and Deep-RIBOmap)—as demonstrations of generalizability across platforms, tissue scales, molecular layers and dimensions, rather than as standalone biological discovery studies. Throughout, comparisons are framed for the task STARComm was designed for: recovery of spatial communication modules, not every form of cell–cell communication inference.

METHODS

STARComm Algorithm

CELLxFEATURE matrix

Consider the set of genes $G = \{g_1, g_2, \ldots g_m\}$, which can be divided into ligand genes $L = \{l_1, l_2, \ldots l_\omega\}$ and receptor genes $R = \{r_1, r_2, \ldots r_\delta\}$. The ligand and receptor genes measured on the spatial transcriptomics panel are $G_{panel} = (L \cup R) \cap G$. The tissue contains a set of n cells, denoted by $S = \{c_1, c_2, \ldots c_n\}$. For single-cell platforms, each observation represents a segmented cell; for Visium HD, each observation represents a spatial bin (8 μm; 2,518,890 bins were analyzed across four sections). The gene expression data collected from these cells is represented by a matrix A of size $n \times m$, where each element a_{ij} indicates the number of transcripts detected for gene *j* in cell *i*.

Ligand-receptor list

Ligand–receptor pairs were obtained by merging CellChat v2 and CellTalkDB (v1.0). The merged resource is denoted $\Pi = \{(l, r): l \in L,\ r \in R\}$, an ordered set in which the ligand is listed first and the receptor second; each pair is indexed by a single symbol $p = (l, r) \in \Pi$. After restricting the resource to genes measured in each dataset and collapsing duplicate pairs and multimeric complexes into single ligand–receptor entries, the number of unique ligand–receptor pairs was panel-dependent (17 pairs for the Xenium cGVHD panel, 250 for the MERSCOPE panel, approximately 3,000 for Visium HD, and 220 for Deep-STARmap/Deep-RIBOmap). The median number of receptors associated with each ligand was 3, and the median number of ligands associated with each receptor was 2; these values were calculated on the full merged resource before dataset-specific panel filtering.

Ligand-receptors Binding Detection

Optimal threshold

A threshold-based approach within the *TACIT* framework was used to identify cells with positive ligand or receptor expression while reducing background noise. STARComm applied this thresholding independently to each ligand and receptor gene and did not require cell-type or cell-state labels, so the binarization neither requires nor depends on prior cell-type annotation[19,20]. The threshold for each gene g_i is defined as a function $\theta(g_i, A)$, where A is the gene expression matrix. In simulations, the TACIT threshold was compared with eight alternative binarization rules—any non-zero count, the 20th, 50th and 90th percentiles, mean + 1 SD, mean + 2 SD, Otsu's method and the interquartile-range fence—applied in the same pipeline (Supplementary Figure 1e).

Ligand-receptor pairs

For each ligand-receptor pair $(l, r) \in \Pi$, identify the set of cells expressing positive levels (above the threshold) of the ligand l and receptor r. Let S_l be the set of cells with positive expression of ligand l, and S_r be the set of cells with positive expression of receptor r. Both S_l and S_r are subsets of the overall cells in S, i.e., $S_l \subseteq S$ and $S_r \subseteq S$.

Next, identify all pairs of cells that represent potential ligand-receptor communications. Specifically, for each pair, the ligand-positive cell $c_l \in S_l$ and the receptor-positive cell $c_r \in S_r$ are considered communication pairs, with $c_l \neq c_r$ so that autocrine (same-cell) events are excluded, if their Euclidean distance is below the search radius Δ. The set of communication events of pair p is therefore:

$$T_p = \{(c_l, c_r): c_l \in S_l,\ c_r \in S_r,\ c_l \neq c_r,\ \| \mathrm{loc}(c_l) - \mathrm{loc}(c_r) \| < \Delta\}$$

where both c_l and c_r are cells with positive expression of ligand l and receptor r, respectively, and their proximity suggests an intercellular communication. The default search radius (Δ) for potential cell-cell communication is set to 50μm. This value was selected as an operational definition of local signaling and evaluated through sensitivity analyses using radii of.

The same radius was used for two- and three-dimensional data. Each detected pair was represented by an inferred communication-event midpoint. This midpoint is a computational representation of the putative communication event and does not establish direct physical contact between the two observations.

It is assumed that each pair (c_l, c_r) corresponds to a contact point $t \in T$, with a location function $t(c_l, c_r)$ defined as the midpoint between the ligand cell c_l and the receptor cell c_r:

$$loc(t) = \frac{loc(c_l) + loc(c_r)}{2},$$

where $loc(t)$ denotes the spatial coordinates of communication t.

Spatial Kernel Density of Ligand Receptors

Neighbors of ligand-receptor pairs

The grid is determined by the size of the bins, measured in micrometers (μm). For a grid with bin size B, the entire tissue is divided into a grid of equally sized intervals, each B μm in both the X and Y directions, ensuring each bin is a B x B μm^2. Next, for each bin, the function $Count\ (c_l, c_r, B)$ calculates the total number of communications for each $(l, r) \in \Pi$ within the bin B. This is determined based on the coordinates of the tissue map. Each communication event is assigned to a single bin according to its midpoint loc(t); the ligand- and receptor-expressing cells themselves need not lie within that bin. The Count function therefore tallies, per bin, the number of L–R events whose midpoints fall inside that bin.

Kernel density estimation

Next, Gaussian kernel density estimation (KDE) is employed to estimate the spatial distribution of communication events across the tissue. A higher density value indicates a greater frequency of communication occurring at that location. Throughout, each ligand–receptor pair is indexed by a single symbol p = (l, r). For each L–R pair p, the densityτ at a bin centre loc(b) is

obtained by summing a Gaussian kernel over the communication events of that pair, with the kernel evaluated on the distance between the bin centre loc(b) and each event midpoint loc(t).

In the 2D case: Let T_p be the set of communication events of pair p, $\mathrm{loc}(t) \in R^2$ the midpoint of event t, and $\mathrm{loc}(b) \in R^2$ the centre of bin b ($b_1, \ldots, b_k$). The density of pair p at bin b is estimated by summing a Gaussian kernel over the event midpoints of that pair:

$$\hat{f}_p(b) = \frac{1}{N_p h^2} \sum_{t \in T_p} K\left(\frac{\mathrm{loc}(b)\text{-}\mathrm{loc}(t)}{h}\right)$$

where:

$N_p = |T_p|$ is the number of communication events of pair p,

$h > 0$ is the bandwidth parameter,

$\mathrm{loc}(t)$ is the midpoint of event t and $\mathrm{loc}(b)$ is the centre of the bin at which the density is evaluated (k bins in total),

The Gaussian kernel function is:

$K(u) = \frac{1}{2\pi} \exp(-\frac{1}{2} u^T u)$.

Because each pair's density profile is z-scored across bins before clustering (see below), the per-pair normalizing constant does not affect MCIM assignment.

In the 3D case: With $\mathrm{loc}(t), \mathrm{loc}(b) \in R^3$ denoting the event midpoint and the voxel centre, the density of pair p is:

$$\hat{f}_p(b) = \frac{1}{N_p h^3} \sum_{t \in T_p} K\left(\frac{\mathrm{loc}(b)\text{-}\mathrm{loc}(t)}{h}\right)$$

where:

- $N_p = |T_p|$ is the number of communication events of pair p,
- $h > 0$ is the bandwidth parameter,
- $\mathrm{loc}(t)$ is the event midpoint and $\mathrm{loc}(b)$ the voxel centre,

- The Gaussian kernel function is:
- $K(u) = \frac{1}{(2\pi)^{\frac{3}{2}}} \exp(-\frac{1}{2} u^T u)$.

Identification of Co-localized L–R Interactions

Densities $\hat{f}_p(b_i)$ are calculated for all ligand–receptor pairs $p \in \Pi$ at every bin b_i. Stacking these profiles yields a bin-by-pair matrix $D \in R^{k \times |\Pi|}$ with $D_{ip} = \hat{f}_p(b_i)$. Each column of D is z-scored across bins so that pairs of different absolute abundance contribute on a common scale.

The Leiden clustering algorithm (leidenalg 0.12.0) is then applied to the matrix D, grouping bin exhibiting similar patterns of high-density communication into clusters, interpreted as Multicellular Communication Interaction Modules. This clustering approach reveals regions with distinct spatial co-location of ligand-receptor activity. Because clustering is performed on bins, each cell is subsequently assigned the MCIM label of the bin that contains it; the cell-level module maps shown in the figures therefore visualize the underlying bin-level clustering.

MCIM Simulation dataset

Let $L = \{l_1, l_2, \ldots l_\omega\}$ be the set of simulated ligand genes, and $R = \{r_1, r_2, \ldots r_\delta\}$ be the set of simulated receptor genes. The set of ligand-receptor pairs is defined as

$$\Pi = \{(l_i, r_j) : l_i \in L,\ r_j \in R\},$$

Each pair lists the ligand first and the receptor second, as in the main framework. The set of cells in the simulated tissue sample is denoted by $S = \{c_1, \ldots, c_n\}$. Each cell $c_i \in S$ is assigned to a ground-truth multicellular communication interaction module (MCIM), which serves as the reference label for clustering evaluation:

$$\kappa: S \to \{1, \ldots, K\}, \quad K = 4$$

Where $\kappa(c_i) = k$ indicates that cell c_i belongs to the kth MCIM. For each MCIM, a subset of ligand-receptor pairs $\{(l_i, r_j)\} \subset \Pi$ is randomly selected to be enriched within that MCIM. Next, the pairwise Euclidean distance between cells ci and c j is calculated as:

$$d_{ij} = \sqrt{(x_i - x_j)^2 + (y_i - y_j)^2}$$

where (x_i, y_i) are the spatial coordinates of cell c_i. Edges (c_i, c_j) representing potential communication links are sampled with a probability that decreases with the spatial distance between cells. Specifically, for each pair (c_i, c_j), the probability of an edge is modeled as:

$$P(\text{edge between } c_i \text{and } c_j) = p_o * \exp(-\frac{d_{ij}}{\lambda})$$

where p_o is a base probability, and λ is a decay parameter that controls how rapidly the probability decreases with distance. In this model, pairs separated by less than 50μm have a higher probability of forming an edge, while pairs beyond 50μm retain a non-zero probability that diminishes exponentially with increasing distance. For each sampled edge (c_i, c_j) that carries communication, ligand or receptor expression levels are assigned. If cell ci carries a ligand/receptor, its expression level for that ligand/receptor gene i is sampled from a Negative Binomial distribution with a high mean:

$$X_i \sim NB(\text{size} = 1, \mu = \mu_H)$$

If the cell does not carry the ligand or receptor, the expression is sampled with a baseline mean:

$$X_i \sim NB(\text{size} = 1, \mu = 2)$$

Hence, in this simulation, the density of cell-cell communication can be regulated by modifying the base probability p_o, the number of ligand-receptor pairs (by adjusting ω or δ), and the high-expression mean μ_H.

Each simulated section contained n = 3,000 cells distributed, with the four MCIMs arranged (Supplementary Figure 1a). Negative Binomial size = 1 with background mean 2. In signal-to-noise experiments, μ_H was varied from 4 to 40 with 10, 20, 50 or 100 ligand–receptor pairs

(Supplementary Figures 1c and 2a,c). In communication-density experiments, the fraction of neighbouring cell pairs carrying active communication was set to 10%, 20%, 40%, 60%, 80% and 100% with $\mu_H = 6$ or 10 and 50 ligand–receptor pairs (Supplementary Figures 1d and 2b). The number of ligand–receptor pairs was varied from 10 to 100 in Supplementary Figure 2d. All methods were run on identical replicates.

Spatial Autocorrelation Analysis using Moran's I

To evaluate whether MCIMs are spatially co-located in the tissue, Moran's I statistic is computed for each MCIM across the spatial domain. Let $S = \{c_1, c_2, \ldots c_n\}$ denote the set of cells, where each cell c_i has spatial coordinates (x_i, y_i). For a given MCIM k, define a binary indicator variable:

$$Z_i^{(k)} = \begin{cases} 1, \text{if cell } c_i \text{ belong to MCIM } k \\ 0, \text{otherwise} \end{cases}$$

Let $W = [w_{ij}]$ be a spatial weights matrix, where w_{ij} reflects the spatial proximity or connection strength between cells c_i and c_j, normalized so that $\sum_{i,j} w_{ij} = 1$. The Moran's I statistic for MCIM k is calculated as:

$$I^{(k)} = \frac{n}{\sum_{i,j} w_{ij}} * \frac{\sum_{i,j} w_{ij}\left(Z_i^k - \overline{Z^k}\right)\left(Z_j^k - \overline{Z^k}\right)}{\sum_{i=1}^{n}(Z_i^k - \overline{Z^k})^2},$$

Where:

- n is the total number of cells,
- $\overline{Z^k} = \frac{1}{n}\sum_{i=1}^{n} Z_i^k$ is the mean of Z^k

Hypotheses:

$$\begin{cases} H_o : \text{The MCIM } k \text{ is spatially randomly distributed (no autocorrelation)} \\ H_a : \text{The MCIM } k \text{ shows positive spatial autocorrelation (clustering)} \end{cases}$$

Significance of the Moran's I value is evaluated through permutation tests, where the labels Z^k are randomly shuffled 1000 times to generate a null distribution. The resulting p-value indicates whether the clustering of MCIM k is statistically significant.

SpatialDM (v0.3.1)

SpatialDM was run as an annotation-free comparator that scores spatial co-expression of ligand–receptor pairs using a bivariate Moran's statistic. Spatial coordinates were supplied to the object and a radial-basis-function spatial weight matrix was constructed (bandwidth l = 1.2, distance cutoff 0.2). Global and local co-expression significance were assessed by permutation testing with Benjamini–Hochberg correction, yielding, for each pair, the spots showing significant local L–R co-expression. To place SpatialDM on the same footing as STARComm, these per-spot significance profiles were then passed into the identical bin-by-feature pipeline (binning, per-pair z-scoring, and Leiden clustering) used for STARComm, so that the two methods were compared on a common downstream representation rather than through method-specific post-processing.0.2, via an RBF kernel to model spatial relationships. Gene interaction data, including ligand-receptor pairs, are stored in adata2.uns under entries like 'geneInter', 'receptor', and 'ligand'. Global spatial association is then evaluated with sdm.spatialdm_global(), testing overall Moran's association across all spots. Significant ligand-receptor pairs are identified using sdm.sig_pairs() with permutation testing and FDR correction. Local co-localization is assessed with sdm.spatialdm_local(), followed by filtering significant spots via sdm.sig_spots(). These significant spots are binarized based on a threshold, and spatial patterns are analyzed with SpatialDE through SpatialDE.run(), executed within a limited BLAS thread context using threadpool_limits(). The resulting spatial patterns are clustered using kmeans(), with a specified number of clusters (e.g., 4), and these labels are used for downstream spatial clustering, such as Leiden clustering, to identify spatially co-localized cell populations.

COMMOT (v0.0.3)

COMMOT was run as an annotation-free comparator that infers directional ligand–receptor signaling using collective optimal transport, which couples ligand and receptor distributions under mass-conservation and spatial-range constraints while accommodating competing species. COMMOT was executed with a 50 μm signaling distance to match the

proximity threshold used by STARComm, producing per-cell sender and receiver signaling scores (the sum-sender and sum-receiver outputs). To ensure a fair comparison, these scores were passed into the same bin-by-feature pipeline (binning, per-pair z-scoring, and Leiden clustering) applied to STARComm and SpatialDM, rather than being clustered by a method-specific procedure.

Spatial Drug2Cell workflow.

Therapeutic relevance of module ligand–receptor programs was assessed with the spatial Drug2Cell pipeline, which maps module receptors to approved drugs and clinical candidates using a curated drug–target reference (ChEMBL_37) and scores per-module druggability from the receptor-expressing bins. Drug–target mappings for all pan-cancer MCIMs are shown in Figure 5g and are reported as hypothesis-generating prioritizations rather than predictions of treatment response.

Calculation of the area of the tissues

Tissue area was computed directly from the cell-centroid coordinates, which are expressed in micrometers for every dataset analyzed. For each tissue, the convex hull of the (x, y) centroids was obtained with chull() in R, and the enclosed area was computed from the ordered hull vertices using the shoelace formula, $A = \frac{1}{2} |\Sigma (x_i y_{i+1} - x_{i+1} y_i)|$. Areas are reported in μm². The convex hull provides an upper-bound approximation of tissue extent and slightly overestimates area for sections with concave boundaries.

Performance metrics

The clustering performance was evaluated using the Adjusted Rand Index (ARI), which quantifies the similarity between the predicted clusters and the simulated true labels in the simulated data. The ARI was calculated using the aricode package version 1.0.3. An ARI score

of 1 indicates perfect agreement, while scores closer to 0 or negative values suggest poor or no agreement. This metric was used to compare the effectiveness of different clustering methods against the simulated ground truth. Furthermore, to assess the spatial coherence of the identified modules, we calculated Moran's I statistic for each MCIM across the spatial domain. This metric evaluates spatial autocorrelation, with higher scores indicating that the communication interaction modules are significantly clustered rather than randomly distributed throughout the tissue.

Statistical Analyses

Statistical analyses and figure generation were performed using R (version 4.3.0). When comparing two groups, a Student's t-test was employed if data met the assumption of normality; otherwise, the non-parametric Wilcoxon rank-sum test was utilized. For comparisons involving more than two groups, analysis of variance (ANOVA) was conducted, followed by post-hoc tests if significant differences were observed. To correct for multiple testing, the false discovery rate was controlled using the Benjamini-Hochberg procedure. Statistical significance was defined as $P < 0.05$, or an adjusted $P < 0.05$ for multiple comparisons.

Ethics and Xenium Experiments

This study included all patients diagnosed with oral chronic graft-versus-host disease (cGVHD) between 2017 and 2023 at the Hospital das Clínicas, School of Medicine, University of São Paulo. Patients were included only if histopathological features of cGVHD were present in the oral mucosa or minor salivary glands. Biopsies that had a clinical diagnosis of cGVHD but lacked histopathological confirmation were excluded. The study involving salivary gland samples from patients with chronic graft-versus-host disease and healthy controls was approved by the Research Ethics Committee of Hospital das Clínicas, Faculdade de Medicina da Universidade de São Paulo (HCFMUSP), under CAAE 65309722.9.0000.0068 and approval number 5.800.37. All participants provided written informed consent prior to inclusion. The study was conducted in

accordance with the Declaration of Helsinki. The dataset comprises samples from 23 patients, totaling 35 tissue specimens and approximately 842,154 cells. A tissue microarray (TMA) was also constructed, containing 17 cGVHD tissues from patients with follow-up data and 6 healthy minor salivary gland tissues. All samples were derived from FFPE tissue blocks, which were melted and re-embedded into a single recipient block to align with the fiducial frame of the Xenium slide (10x Genomics). Spatial transcriptomic analysis was performed using the standard 280-plex human breast cancer panel from 10x Genomics, following the manufacturer's protocol[22]. The slides were then stored in 10% glycerol in PBS for 7 days and subsequently processed using the PhenoCycler Fusion pipeline[36]. Clinical trial number: not applicable.

RESULTS

STARComm: an annotation-free framework for discovering multicellular communication modules

STARComm resolves higher-order multicellular communication modules directly from spatial transcriptomics data. In many complex diseases, pathology arises from spatially organized dysregulation of tissue signaling; we first outline the framework and then benchmark it on simulated and experimental tissues. Central to this pathology is cell–cell communication (CCC), a process rarely driven by a single ligand–receptor (L-R) pair. Instead, multiple signaling pathways operate concurrently within a shared tissue microenvironment, forming complex interaction landscapes (Figure 1a)[21]. To impose biological and spatial structure on this complexity, we introduce the concept of Multicellular Communication Interaction Modules (MCIMs). We define MCIMs as spatially discrete hotspots of coordinated signaling that represent emergent functional units of multicellular cooperation (Figure 1d). MCIMs are related to, but distinct from, cellular neighborhoods or tissue "ecotypes": neighborhoods are defined by local cell-type composition, whereas MCIMs are defined by the joint spatial density of L–R communication events and are detected without cell-type labels. Cell-type composition is used only afterwards, to interpret each module.

To identify and characterize MCIMs from spatial transcriptomic data, we developed STARComm, a computational framework built upon a rigorous three-step process. First, STARComm identifies high-confidence communication edges between individual cells. This step pinpoints potential interactions by locating signal-sending (ligand-expressing) and signal-receiving (receptor-expressing) cells based on both gene expression and spatial proximity. To maximize the accuracy of this step, we leverage the optimal thresholding algorithm from TACIT to establish context-aware expression cutoffs for each gene (Figures 1e-f)[19,20]. This data-driven approach avoids the use of arbitrary global thresholds, thereby minimizing false positives arising

from background noise or data sparsity. A communication edge is subsequently established between a positive ligand-cell and a corresponding positive receptor-cell if they fall within a defined spatial distance, resulting in a comprehensive map of pairwise connections (Figure 1f).

In the second step, these discrete communication edges are transformed into continuous spatial density maps to model the tissue's underlying "signaling landscape". This transformation creates a spatially coherent representation that allows for integrating diverse L-R pairs. Using kernel density estimation (KDE), the local abundance of each interaction type is quantified across a discretized tissue grid (Figures 1g-h). Each interaction is anchored spatially at the midpoint between the sending and receiving cells, providing an operational spatial location for the signaling event. This process converts the set of discrete cell-cell interactions into a smooth, continuous density map for each L-R pair, where high-intensity regions denote areas of concentrated signaling activity.

Finally, the third step integrates these individual density maps to discover and define the MCIMs. To ensure that all interactions contribute equitably to the final result, the density maps are first normalized using a z-score transformation (Figure 1i). This crucial step places the densities of all L-R pairs, regardless of their absolute abundance, onto a common scale, preventing highly prevalent interactions from dominating the analysis. The normalized maps are then concatenated into a feature matrix where each row represents a spatial bin and each column an L-R pair, capturing the complete communication profile at every location. Leiden clustering of a nearest-neighbour graph of bins is then applied to this matrix (Methods), which groups spatial bins with similar communication profiles (Figure 1j). This data-driven approach reveals emergent patterns of co-localized signaling pathways, thereby defining the boundaries and composition of the MCIMs (Figure 1k). Through this framework, STARComm provides a scalable methodology for resolving the architecture of multicellular communication at cell or bin resolution, enabling the discovery of tissue-scale immunologic structures not evident from cell-type annotations or single-pair interactions alone (Figures 1l-n).

STARComm recovers simulated communication modules with higher accuracy, spatial coherence and speed

To evaluate whether STARComm can recover spatially organized communication modules when the ground truth is known, we developed a simulation framework with predefined spatial communication regions. Our framework generated synthetic tissue sections comprising 3,000 cells, which were partitioned into four distinct, ground-truth multicellular communication interaction modules (MCIMs) (Supplementary Figure 1a). The communication profile of each MCIM was governed by three key parameters: a unique set of active ligand-receptor pairs, the communication density, and the gene expression distribution of the corresponding ligands and receptors. Communication density was quantified as the fraction of active ligand-receptor interactions among all neighboring cells, defined as those within a 50μm distance threshold. To emulate realistic expression patterns, we modeled gene expression levels using a mixture of negative binomial distributions, which effectively distinguishes the elevated expression in communicating cells from the basal expression in non-communicating cells (Supplementary Figure 1b). Simulation parameters, replicate numbers and random seeds are given in Methods.

Because existing methods are not designed to directly identify multicellular communication modules, we adapted their cell-level or ligand-receptor-level communication features for benchmarking against the simulated MCIM labels. Specifically, COMMOT sender/receiver signaling scores, SpatialDM local bivariate Moran's I significance profiles, and an expression-only baseline (ExpressionOnly) that clusters cells on ligand–receptor expression without spatial information were each passed through the same binning, z-scoring and Leiden clustering used for STARComm[10,11,19]. Because COMMOT and SpatialDM were designed for other communication tasks (directional signaling and pairwise spatial co-expression, respectively), this benchmark evaluates their suitability for module recovery only. To evaluate performance, we designed two primary simulation experiments. First, to test robustness against noise, we varied

the signal-to-noise ratio by fixing the mean expression for non-communicating cells at 2 and varying the mean for communicating cells from 4 to 40 (Supplementary Figure 1c). Second, we varied communication density, defined as the fraction of neighbouring cell pairs within each MCIM that carry active L–R communication (Supplementary Figure 1d).

In the first test assessing signal-to-noise, STARComm consistently achieved the highest Adjusted Rand Index (ARI). Critically, at the lowest signal-to-noise ratio where other methods failed, STARComm was the only method to effectively capture the simulated ground-truth MCIMs (mean-ARI=0.40, SD=0.13), demonstrating its superior sensitivity (Supplementary Figures 1c and 2a). We further compared the TACIT optimal threshold against a panel of alternative binarization methods (non-zero, 20th/50th/90th percentile, mean + 1 SD, mean + 2 SD, Otsu, and IQR fence), and found that the TACIT optimal threshold yielded the highest ARI (Supplementary Figure 1e). In the second test, we varied the probability of communication from 10% to 100% in each MCIM to evaluate performance as a function of communication density (Supplementary Figure 1d). Here, STARComm maintained a high ARI of 0.7 even at the lowest communication density (10%), outperforming ExpressionOnly (ARI=0.20), COMMOT (ARI=0.01), and SpatialDM (ARI=0.01) at the same challenging level. This result highlights STARComm's unique ability to detect sparse communication patterns. In terms of computational efficiency, STARComm demonstrates a substantial advantage, with a mean runtime of just 12.63 seconds (SD=10s). STARComm was approximately 237 times faster than SpatialDM (mean ≈ 2994s), and 463 times faster than COMMOT (mean ≈ 5852s) (Supplementary Figure 1f). This two-order-of-magnitude reduction in runtime establishes STARComm as a highly scalable solution for analyzing large spatial datasets. Visual inspection of a representative spatial plot from the low-density simulation confirms that STARComm better captures the co-localization of interacting cells (Supplementary Figure 1g). We quantified this spatial coherence using Moran's I, which confirmed STARComm's MCIMs were significantly more spatially autocorrelated (mean Moran's I = 0.94) than those from all other methods (Supplementary Figure 1h)[23]. STARComm also achieved the highest ARI across

simulations with 20 and 100 ligand–receptor pairs (Supplementary Figure 2a), across communication densities and signal-to-noise settings with 50 pairs (Supplementary Figure 2b,c), and when the number of pairs was varied from 10 to 100 (Supplementary Figure 2d). Finally, we assessed sensitivity to the KDE bandwidth. ARI remained above approximately 0.5 across the bandwidths tested (approximately 50–700 μm), with the highest values at small bandwidths and a progressive decline at larger bandwidths (Supplementary Figure 2e). This combination of accuracy, speed, and robustness supports STARComm's application to large-scale spatial transcriptomics datasets and cohort-level analyses.

STARComm produces spatially focal modules and shorter runtimes than comparators in a Xenium tissue benchmark

To evaluate STARComm in a real single-cell spatial transcriptomics dataset with recognizable tissue organization, we analyzed a representative chronic graft-versus-host disease (cGVHD) minor salivary gland biopsy profiled by Xenium. This tissue contained organized immune aggregates resembling tertiary lymphoid structures (TLS), which provide a biologically relevant benchmark because TLS formation is driven by coordinated interactions among multiple immune, stromal and vascular cell populations within a spatially confined niche. Thus, TLS-like regions offer an appropriate real-tissue context for evaluating whether STARComm can detect higher-order multicellular communication modules rather than diffuse or isolated ligand-receptor signals.

We compared STARComm with COMMOT and SpatialDM on the same tissue section. Because COMMOT and SpatialDM were not designed to identify MCIMs directly, we compared the spatial organization and biological enrichment of their inferred communication-derived clusters. STARComm identified a discrete communication module that was spatially confined to anatomically coherent TLS-like regions, whereas COMMOT- and SpatialDM-derived assignments were more diffuse and extended across broader tissue areas (Figure 2a–b). Quantitatively,

STARComm clusters showed significantly greater above-chance spatial concentration than those from COMMOT or SpatialDM using Moran's I (Figure 2c).

The spatial focality of STARComm was accompanied by improved biological specificity. The STARComm TLS-associated module was enriched for canonical TLS-related immune populations, including B cells, $CD4^+$ T cells, $CD8^+$ exhausted T cells, dendritic cells, and plasma cells, capturing 34.9% of TLS-associated immune cells. In comparison, the corresponding top-enriched clusters from SpatialDM and COMMOT captured 19.2% and 20.8% of TLS-associated immune cells, respectively (Figure 2d). STARComm also completed the analysis in approximately 5 minutes, compared with approximately 24 hours for SpatialDM and 36 hours for COMMOT (Figure 2e). These results indicate that STARComm can identify spatially focal and biologically interpretable communication modules in real tissue while substantially reducing computational runtime.

STARComm generalizes to a multi-sample Xenium cohort and detects condition-associated modules

We next tested whether STARComm generalizes from a single section to a multi-sample cohort, and whether module proportions distinguish tissue conditions. We used chronic graft-versus-host disease (cGVHD), a major cause of late non-relapse mortality after allogeneic hematopoietic cell transplantation[24,25] (Figure 3a), as a test case. The cohort included 17 cGVHD patients and 6 healthy individuals (Figure 3b). The minor salivary gland biopsies (27 cGVHD samples and eight healthy samples) were processed through our standardized spatial transcriptomics pipeline, profiled using a targeted 280-plex in-situ hybridization (ISH) panel on the Xenium platform. This panel included probes for 17 key ligand–receptor pairs and yielded a dataset of 842,154 spatially resolved cells across 35 tissues (Figure 3b-d).

Having validated STARComm's performance, we then performed an integrated STARComm analysis across all tissues and ligand-receptor pairs to identify shared and divergent

spatial communication patterns between healthy and GVHD. This integrated analysis enabled us to identify communication programs shared across cGVHD salivary gland specimens and distinguish them from patterns observed in healthy tissues. STARComm detected nine MCIMs across the 35 tissues (Figure 3e–f). Coloring the integrated embedding by patient (Figure 3e) was used to assess whether modules were driven by individual patients. These MCIMs reflect densely interacting, spatially coherent neighborhoods of immune, stromal, and vascular cells engaged in active signaling. A heatmap of communication density illustrates the co-location of multiple cell-cell communication events within the MCIMs (Figure 3g). The proportion plot illustrates two tissue conditions across 35 tissues, demonstrating the strong enrichment of several MCIMs in the GVHD cohorts (Figure 3h). Cell type composition analysis further revealed that each MCIM comprises distinct combinations of cell types, consistent with MCIMs being higher-order patterns of multicellular, coordinated signaling (Figure 3i).

To determine the relationship between cell type tissue architecture and cellular communication, we performed cell type annotation using TACIT[19]. Figure 4a shows the spatial distribution of annotated cell types in representative cGVHD and healthy tissues. Of particular interest were the TLS-like regions characterized by dense immune-cell aggregates. STARComm robustly captured these intralesional communication hubs, most notably MCIM-0, characterized by elevated signaling among B cells, T cells, fibroblasts, and vascular endothelial cells (Figure 3i). Notably, this MCIM aligns with the benchmarking-derived Cluster 0 identified in our single-sample comparison, supporting the reproducibility of its biological coherence. A closer examination of ligand-receptor maps showed distinct communication patterns between healthy and diseased regions. For example, CD86::CTLA4, CD274::CD80, CCL5::SDC4 are highly enriched in GVHD samples underlying the communication of cells in the TLS region but are almost entirely absent in healthy tissue, while CDH1::EGFR was detected predominantly in healthy tissues and histologically preserved regions of cGVHD tissues but was absent from TLS-like regions (Figures 4b–c)[25].

MCIM proportions differed between healthy and cGVHD tissues (Figure 4e), and principal component analysis of MCIM proportions separated the two conditions (Figure 4f). cGVHD tissues showed significantly elevated communication density per unit area (Figure 4g), consistent with increased cell–cell crosstalk in cGVHD. MCIM-0 and MCIM-2 were more frequent in cGVHD than in healthy tissues, whereas MCIM-6 was more frequent in healthy tissues (Figure 4h). Key upregulated ligand-receptor pairs within these MCIMs, particularly those associated with tertiary lymphoid structures, included complement activation (C1QA::CD93), immune checkpoint regulation (CD274::CD80; CD86::CTLA4), immune cell recruitment (CXCL12::CXCR4; CXCL12::CD4) and endothelial/matrix interactions (MMP2::PECAM1) (Figure 4i)[26–30]. Thus, in this cohort, STARComm detected differences between conditions at the level of multicellular modules as well as individual pairs.

These module-level differences are consistent with recognized features of cGVHD, including immune activation, lymphocyte recruitment and stromal remodeling. Several of the enriched axes (CD274::CD80, CD86::CTLA4, CXCL12::CXCR4, C1QA::CD93 and MMP2::PECAM1) involve pathways with existing or investigational modulators[26,27,31–34]. We present these as hypothesis-generating examples of how MCIM output can prioritize candidate axes for validation in independent cohorts, not as evidence of therapeutic relevance.

STARComm scales to a 16-region, eight-cancer MERSCOPE dataset

To test scalability to atlas-scale data and generalization across tumor types, we applied the framework to a publicly available MERSCOPE cancer atlas from the Vizgen repository[36]. This dataset comprised 16 spatial tissue regions representing eight cancer types. In total, the dataset contained over 14.5 million cells, a 500-gene panel, and 250 ligand-receptor pairs. Application of the STARComm framework to this dataset identified 24 distinct multicellular communication interaction modules (MCIMs), revealing both unique and shared communication patterns across the different cancer types (Figure 5a, Supplementary Figure 3a–c)

A Uniform Manifold Approximation and Projection (UMAP) analysis of MCIM proportions revealed distinct patterns of enrichment corresponding to specific cancer types (Figure 5b). This analysis effectively segregated the tumors based on their dominant communication modules. For example, while cancers like colon (MCIM-6), liver (MCIM-4), and lung (MCIM-15) were defined by single, dominant modules, others such as breast (MCIMs-8, 11), ovarian (MCIMs-5, 10), and uterine (MCIMs-16, 19) cancers displayed more complex signatures involving multiple MCIMs (Figure 5c).

MCIM-3 (labelled Fibro–Immune 3 in Figure 5) recurred across several cancer types, including melanoma, prostate and uterine tumors (Figure 5a; Figure 6f). We describe it as an immune-regulatory module rather than as immunosuppressive or immune-activating, because its features point in both directions: in the pan-cancer analysis it was enriched for KEGG terms including primary immunodeficiency, the intestinal immune network for IgA production and viral protein interaction with cytokines and cytokine receptors (Figure 5f), and in the uterine section it was characterized by TGF-β-family signaling together with GO terms for positive regulation of leukocyte activation and cell adhesion (Figure 6g,i)[26,39,40]. Spatial mapping of selected tumor-associated pairs, TGFB1::ENG in melanoma and TGFB1::TGFBR3 in prostate cancer, illustrates how individual axes within such modules can be localized for follow-up (Figure 5e).

To illustrate how module output can be linked to existing drug–target annotations, we mapped module ligand–receptor pairs with spatial Drug2Cell (Figure 5g). For instance, MCIM-4, detected in both liver cancer samples (Figure 5d), was characterized by enrichment of VTN::KDR; KDR is a target of sorafenib[41,42]. These mappings are hypothesis-generating and do not indicate treatment response.

STARComm yields more spatially coherent modules than comparators in a uterine cancer benchmark and scales to the whole section

Given the computational scale of the full MERSCOPE dataset, direct full-tissue benchmarking against COMMOT and SpatialDM was not feasible. We therefore selected a smaller uterine cancer region of interest (~6,000 cells) to compare spatial coherence, biological interpretability and runtime across methods. Even within this constrained subset, STARComm resolved more spatially coherent intra-tumoral communication patterns than COMMOT and SpatialDM (Figures 6a,b). Specifically, STARComm identified two region-of-interest clusters: cluster 0, characterized by angiogenic and growth signaling (VEGFA::NRP1, VEGFA::ITGB1 and VEGFA::KDR), and cluster 1, defined by cell adhesion and migration pairs (e.g., ICAM3::ITGB2, VCAM1::ITGA4, VCAM1::ITGB1, VCAM1::ITGB2, and COL1A1::ITGA5) (Figure 6c).

The spatial coherence of these discoveries was validated by Moran's I scores; STARComm achieved a score of 0.91, indicating high spatial clustering, whereas COMMOT and SpatialDM yielded lower scores of 0.19 and 0.13, respectively (Figure 6d). Furthermore, STARComm exhibited greater computational efficiency, processing the 6,000-cell subset in just 2 minutes, compared to 25 minutes for SpatialDM and 19 hours for COMMOT (Figure 6e). These results indicate that STARComm can resolve intra-tumoral communication heterogeneity with high spatial coherence and substantially reduced runtime in this benchmark.

Beyond these metrics, a primary advantage of STARComm lies in its scalability. Because alternative methods were not practical for whole-slide or large-scale pan-cancer analysis in this study, they could not be used to characterize the full spectrum of cancer-specific communication or intra-tumor heterogeneity. When applied to the entire tissue sample, STARComm revealed three large, spatially distinct regions defined by distinct multicellular communication interaction modules — MCIM-1, MCIM-3, and MCIM-16 (Figure 6f) — each associated with a distinct biological program. MCIM-1 was characterized by WNT5A::FZD7 and enriched for developmental GO terms (for example, digestive tract development and central nervous system neuron differentiation); MCIM-3 by TGF-β-family pairs (TGFB1::TGFBR1, TGFB1::ENG, TGFB1::ITGB1, TGFB1::CAV1 and TGFB1::CXCR4) together with HGF::ITGB1, HGF::NRP1 and

COL1A1::ITGA5, and by GO terms for leukocyte activation and cell adhesion[37-39]; and MCIM-16 by CEACAM1::EGFR, ICAM1::MUC1 and ICAM1::EGFR, with GO terms for leukocyte chemotaxis and myeloid leukocyte migration (Figure 6f–i)[43-45]. MCIM-16 was dominated by tumor-cell–associated cell-type pairs, whereas MCIM-3 involved immune, stromal and vascular pairs (Figure 6h).

Together, the pan-cancer and uterine analyses show that STARComm scales to atlas-scale imaging data, that its advantage in spatial coherence over comparators observed in simulations holds in tumor tissue, and that the resulting modules can be compared across cancer types and used to generate hypotheses about spatially organized tumor microenvironment programs.

STARComm scales to 2.5 million Visium HD bins

To test STARComm on a sequencing-based, near-whole-transcriptome platform, we downloaded and integrated four publicly available datasets from 10x Genomics, analyzing a total of 2,518,890 spatial bins to interrogate approximately 3,000 ligand–receptor pairs. Communication per tissue area was higher in tumor than in normal adjacent tissue (P = 0.017, Supplementary Figure 4b)[46]. Moreover, we identified MCIM 6, a distinct multicellular interaction module positioned at the tumor periphery. (Supplementary Figure 4f). MCIM-6 was characterized by communication among cancer-associated fibroblasts (CAFs), endothelial cells, tumor cells, pericytes, and macrophages, cell types known to modulate tumor growth, angiogenesis and immune responses (Supplementary Figure 4g). Further investigation revealed key L-R interactions within MCIM-6, including *FBN1*::*ITGAV*, *THBS2*::*ITGA6*, *MMP2*::*FGFR1*, *CCL14*::*ACKR1*, and *COL1A1/A2*::*FLT4*, which were implicated in matrix remodeling, angiogenesis, immune modulation, and lymphatic vessel formation (Supplementary Figure 4d). The emergence of MCIM-6 at the tumor-stromal interface identifies a spatially organized

communication hub containing signaling pathways associated with matrix remodeling, vascular biology, and immune regulation.

STARComm extends to three-dimensional transcriptomic and translatomic volumes

To test whether STARComm extends to volumetric data and to a second molecular layer, we applied it to a previously published 3D mouse-brain dataset consisting of Deep-STARmap transcriptomic and Deep-RIBOmap translatomic data[47]. This volumetric dataset comprised 362,704 cells across a 150-μm-thick tissue volume, profiling 1,100 genes including 220 ligand-receptor pairs. Moving beyond conventional 2D slice-by-slice analysis, STARComm successfully identified nine spatially organized multicellular communication interaction modules (MCIMs) within this 3D tissue architecture (Figure 7a,b).

Comparative analysis between transcriptome and translatome revealed both convergence and divergence in their 3D communication landscapes. While the two molecular layers showed significant correlation (Pearson r = 0.64 across 218 ligand–receptor pairs; Figure 7d), the transcriptome exhibited substantially higher overall communication density than the translatome (Figure 7c). Quantitative comparison demonstrated that 91% (198 of 218) of communication interactions were shared between both layers, while 9% (20 pairs) were exclusive to the transcriptomic layer (Figure 7c), suggesting layer-specific signaling mechanisms that may be subject to translational regulation.

At the level of individual pairs, VIP::VIPR1 and CRH::VIPR1 scored higher in the transcriptome, whereas CCK::CCKBR, SST::SSTR1 and CORT::SSTR1 scored higher in the translatome (Figure 7d). To evaluate the effect of reducing the 3D volume to conventional tissue sections, we virtually sectioned the tissue at 5-μm intervals along the z-axis. Collectively, the virtual 2D sections retained 6,311 communication events, compared with 90,583 events detected in the complete 3D volume, approximately 7% of the volumetric total (Figure 7e). This reduction reflects the loss of

inferred communication events spanning different z-planes when the tissue is analyzed as separate 2D sections.

These results show that STARComm runs natively on 3D coordinates, that analysis of the full volume recovers substantially more communication events than slice-by-slice analysis, and that it can compare communication architecture across paired molecular layers.

DISCUSSION

STARComm was developed to address a central limitation in spatial cell-cell communication analysis: the need to move beyond individual ligand-receptor pairs toward spatially organized, higher-order communication programs. Existing methods have substantially advanced the field by incorporating spatial proximity, modeling signaling directionality, or identifying spatially co-expressed ligand-receptor pairs. However, many remain focused on pairwise interactions, depend on cell-type annotations, or face scalability constraints when applied to large spatial transcriptomics datasets. STARComm provides a complementary framework by identifying multicellular communication interaction modules (MCIMs), defined as spatially coherent tissue regions in which multiple ligand-receptor interactions are jointly enriched. This design enables STARComm to capture coordinated signaling neighborhoods rather than isolated communication events.

A key advantage of STARComm is its global-to-local strategy. By first identifying cell-level ligand-receptor proximity events, transforming these events into spatial density profiles, and then clustering co-localized signaling patterns, STARComm converts sparse pairwise interaction signals into interpretable multicellular modules. This strategy supports efficient analysis while preserving spatial information, making it suitable for modern spatial platforms containing hundreds of thousands to millions of cells, bins, or spots. Importantly, STARComm does not require cell-type annotation for MCIM detection, thereby reducing dependence on upstream clustering and annotation choices. However, segmentation and other platform-specific preprocessing decisions can still influence the underlying expression matrix and spatial coordinates. Cell-type labels can instead be used downstream to interpret the cellular composition and biological function of each module. This separation between module discovery and biological interpretation is particularly useful for heterogeneous tissues, where communication programs may not align cleanly with predefined cell states or canonical cell-type boundaries. This design also distinguishes MCIMs

from cellular neighborhoods, which group regions by cell-type composition. Because MCIMs are defined by co-localized communication density, two regions with similar composition can fall into different MCIMs if their signaling differs.

The benchmarking and application studies presented here support a specific claim: for the recovery of spatial communication modules, STARComm improves accuracy, spatial coherence and computational performance relative to the comparators tested, across 2D and 3D datasets. In simulation experiments with known ground truth, STARComm more accurately recovered spatially organized communication modules than COMMOT, SpatialDM, and the expression-only baseline after their outputs were adapted to a common MCIM clustering framework, with particularly strong performance under low signal-to-noise and sparse communication conditions. This advantage extended to experimental tissue: in the Xenium and MERSCOPE benchmarks, STARComm identified spatially focal MCIMs that aligned with recognizable tissue structures and disease-associated microenvironments, while alternative approaches produced more diffuse or less spatially resolved communication patterns. These gains were accompanied by substantial reductions in runtime, allowing STARComm to move beyond small regions of interest and support whole-tissue and cohort-scale analyses. This combination of spatial specificity, biological interpretability, and computational scalability is essential for modern spatial studies, where the key challenge is not only to detect ligand–receptor activity, but to resolve coordinated multicellular communication programs across large and heterogeneous tissues. The successful application of STARComm across MERSCOPE, Xenium, Visium HD, Deep-STARmap, and Deep-RIBOmap further supports its flexibility across imaging-based, sequencing-based, and volumetric spatial platforms, underscoring its general utility for studying multicellular communication architecture in both two-dimensional and three-dimensional tissue contexts. The application of STARComm to Deep-STARmap transcriptomic and Deep-RIBOmap translatomic data further demonstrated its ability to identify shared and molecular-layer-associated communication patterns within intact 3D tissue volumes.

The four application datasets were chosen as demonstrations of generalizability across platforms, scales and dimensions rather than as standalone biological studies, and the biological observations should be read in that light. In cGVHD salivary glands, STARComm identified recurrent immune, stromal, and vascular communication programs, including a module concentrated within TLS-like immune aggregates and modules that differed between cGVHD and healthy tissues. These findings suggest that cGVHD-associated tissue remodeling involves coordinated communication programs rather than isolated signaling axes, although their mechanistic and clinical relevance requires validation in independent cohorts. Across the pan-cancer dataset, STARComm identified both recurrent and cancer-associated MCIMs, including programs related to immune regulation, angiogenesis, stromal remodeling, and tumor–stromal interfaces. Drug–target mapping connected selected module receptors to existing therapeutic agents, but these associations should be interpreted as prioritization hypotheses rather than evidence of treatment response.

The 3D mouse-brain analysis extended this framework beyond conventional tissue sections. Most detected ligand–receptor interactions were shared between the Deep-STARmap transcriptomic and Deep-RIBOmap translatomic layers, while differences in communication density and spatial localization identified molecular-layer-associated patterns. Virtual sectioning retained only a small fraction of the communication events detected in the complete tissue volume, demonstrating that dimensionality can materially influence inferred communication architecture. Together, these applications support MCIMs as interpretable units for comparing spatial signaling across tissue states, diseases, molecular layers, and dimensional contexts.

Several limitations should be considered when interpreting STARComm results. First, STARComm infers putative communication from ligand–receptor expression and spatial proximity; it does not directly measure ligand binding, receptor activation, signaling directionality, or downstream pathway activity. Moreover, the use of a common interaction radius does not

capture the distinct physical ranges of contact-dependent and diffusible signaling processes. Mechanistic conclusions therefore require orthogonal or perturbational validation.

Second, detected MCIMs are constrained by the gene coverage, sensitivity, segmentation accuracy, and spatial resolution of the underlying platform, particularly for targeted imaging panels in which relevant ligand–receptor pairs may be absent. Parameters including expression thresholds, interaction radius, kernel bandwidth, bin size, and clustering resolution can also influence the spatial scale and granularity of the resulting modules.

Third, COMMOT and SpatialDM were not designed to identify MCIMs directly, and their outputs were adapted to a common downstream clustering framework for comparison with STARComm. These benchmarks therefore evaluate their suitability for the specific task of MCIM recovery rather than establish superiority across all forms of cell–cell communication analysis. Full-scale comparisons were also limited when comparator methods could not complete analyses within the available computational resources. CellNEST could not be benchmarked within the prespecified runtime limit using its recommended settings, and other recent methods were not evaluated.

Fourth, the biological applications were retrospective and largely exploratory. The cGVHD findings were derived from a single-center cohort, the pan-cancer analyses included limited numbers of specimens per cancer type, and the 3D transcriptomic and translatomic analysis used a previously published mouse-brain dataset. Independent cohorts, additional tissues, and experimental perturbations will be required to establish the reproducibility, biological mechanisms, and clinical relevance of individual MCIMs. Although MCIM discovery is annotation-free, biological interpretation continues to depend on reliable cell-type annotations, marker validation, and domain expertise. Therapeutic and biomarker associations should therefore be considered hypothesis-generating.

In summary, STARComm provides a scalable, annotation-free approach for resolving multicellular communication architecture from two- and three-dimensional spatial transcriptomic

and translatomic data. By identifying MCIMs, STARComm shifts the analytical focus from isolated ligand–receptor pairs to coordinated spatial communication programs that reflect the multicellular organization of tissues. Its computational efficiency and compatibility across imaging-based, sequencing-based, and volumetric datasets support its use in large-scale studies of tissue organization and disease. With independent validation and continued methodological development, MCIM-based analysis may help connect spatial communication patterns with disease mechanisms and prioritize candidate biomarkers and therapeutic hypotheses.

Code availability:

The code used to develop the STARComm, perform the analyses and generate results in this study is publicly available and has been deposited in https://github.com/huynhkl953/STARComm.

Data availability:

The MERSCOPE dataset can be downloaded via https://info.vizgen.com/ffpe-showcase. VisiumHD can be downloaded via https://www.10xgenomics.com/products/visium-hd-spatial-gene-expression/dataset-human-crc. Other datasets will be available upon request.

Contributions:

For this study, JL and KMB conceptualized the project. JL and KLAH designed the algorithm. KLAH implemented the algorithm and conducted benchmarking experiments. BFM performed manual assessment of GVHD clinical outcome. DDS, GF, LAVSJ, LFFDS, and VGR, supported the recruitment of patients and collected data. KLAH, XZ, BFM, DDS, GF, LAVSJ, LFFDS, VGR, KMB, and JL performed experimental and/or bioinformatic analysis that supported project development. JL, KMB, KLAH, and BFM wrote the original draft; KLAH, XZ, BFM, DDS, GF, LAVSJ, LFFDS, VGR, EG, KMB, and JL critically reviewed and edited the final manuscript.

Conflict of interest:

The authors had access to the study data and reviewed and approved the final manuscript. Although the authors view each of these as noncompeting financial interests, KMB and BFM are active members of the Human Cell Atlas; Furthermore, K.M.B. is a scientific advisor at Arcato Laboratories (Durham, NC) as well as the CEO and co-founder of Stratica Biosciences (Durham, NC); JL is a CTO and co-founder of Stratica Biosciences. All other authors declare no competing interests.

Acknowledgements:

K.M.B. discloses support for the research of this work from the ADA Science & Research Institute (generous start-up funds; Volpe Research Scholar Award), the VCU Department of Oral and Molecular Craniofacial Biology, Philips Institute for Oral Health Research (start-up funds) and the VCU Massey Comprehensive Cancer Center (Harrison Scholar); and NIH/NIDCR 1RM1DE035338. The work also benefited from the VCU Wright Regional Center for Clinical & Translational Science (CCTS) Clinical and Translational Science Award (CTSA) UM1TR004360 to JL and NIH-NCI Cancer Center Support Grant P30 CA016059.

REFERENCES

1. Almet, A. A., Cang, Z., Jin, S. & Nie, Q. The landscape of cell-cell communication through single-cell transcriptomics. *Curr. Opin. Syst. Biol.* **26**, 12–23 (2021).
2. Armingol, E., Officer, A., Harismendy, O. & Lewis, N. E. Deciphering cell–cell interactions and communication from gene expression. *Nat. Rev. Genet.* **22**, 71–88 (2021).
3. Su, J. *et al.* Cell–cell communication: new insights and clinical implications. *Signal Transduct. Target. Ther.* **9**, 196 (2024).
4. Jin, S. *et al.* Inference and analysis of cell-cell communication using CellChat. *Nat. Commun.* **12**, 1088 (2021).
5. Browaeys, R., Saelens, W. & Saeys, Y. NicheNet: modeling intercellular communication by linking ligands to target genes. *Nat. Methods* **17**, 159–162 (2020).
6. Efremova, M., Vento-Tormo, M., Teichmann, S. A. & Vento-Tormo, R. CellPhoneDB: inferring cell–cell communication from combined expression of multi-subunit ligand–receptor complexes. *Nat. Protoc.* **15**, 1484–1506 (2020).
7. Dimitrov, D. *et al.* LIANA+ provides an all-in-one framework for cell–cell communication inference. *Nat. Cell Biol.* **26**, 1613–1622 (2024).
8. Hou, R., Denisenko, E., Ong, H. T., Ramilowski, J. A. & Forrest, A. R. R. Predicting cell-to-cell communication networks using NATMI. *Nat. Commun.* **11**, 5011 (2020).
9. Baruzzo, G., Cesaro, G. & Di Camillo, B. Identify, quantify and characterize cellular communication from single-cell RNA sequencing data with *scSeqComm*. *Bioinformatics* **38**, 1920–1929 (2022).
10. Cang, Z. *et al.* Screening cell–cell communication in spatial transcriptomics via collective optimal transport. *Nat. Methods* **20**, 218–228 (2023).

11. Li, Z., Wang, T., Liu, P. & Huang, Y. SpatialDM for rapid identification of spatially co-expressed ligand–receptor and revealing cell–cell communication patterns. *Nat. Commun.* **14**, 3995 (2023).
12. Shao, X. *et al.* Knowledge-graph-based cell-cell communication inference for spatially resolved transcriptomic data with SpaTalk. *Nat. Commun.* **13**, 4429 (2022).
13. Yan, L., Cheng, J., Nie, Q. & Sun, X. Dissecting multilayer cell-cell communications with signaling feedback loops from spatial transcriptomics data. *Genome Res.* **35**, 1400–1414 (2025).
14. Ji, B., Xu, L. & Peng, S. SpaCCC: Large language model-based cell-cell communication inference for spatially resolved transcriptomic data. Preprint at https://doi.org/10.1101/2024.02.21.581369 (2024).
15. Wu, D. & Datta, S. TWCOM: an R package for inference of cell–cell communication on spatially resolved transcriptomics data. *Bioinforma. Adv.* **4**, vbae101 (2024).
16. Zohora, F. T. *et al.* CellNEST reveals cell–cell relay networks using attention mechanisms on spatial transcriptomics. *Nat. Methods* https://doi.org/10.1038/s41592-025-02721-3 (2025) doi:10.1038/s41592-025-02721-3.
17. Bressan, D., Battistoni, G. & Hannon, G. J. The dawn of spatial omics. *Science* **381**, eabq4964 (2023).
18. Marx, V. Method of the Year: spatially resolved transcriptomics. *Nat. Methods* **18**, 9–14 (2021).
19. Huynh, K. & Liu, J. Deconvolution of Cell Types and States in Spatial Multiomics Utilizing TACIT. (2025).

20. Huynh, K. A novel statistical learning framework to uncover clinically significant spatial ecotypes with single cell spatial multiomics data. *VCU Theses and Dissertations* (VCU Libraries, 2025). doi:10.25772/B6CJ-MR64.
21. Lu, T., Ang, C. E. & Zhuang, X. Spatially resolved epigenomic profiling of single cells in complex tissues. *Cell* **186**, 2275–2279 (2023).
22. Fernandes Matuck, B. *et al.* The Immunoregulatory Architecture of the Adult Oral Cavity. *BioRxiv Prepr. Serv. Biol.* 2024.12.01.626279 (2024) doi:10.1101/2024.12.01.626279.
23. Chen, Y. Spatial autocorrelation equation based on Moran's index. *Sci. Rep.* **13**, 19296 (2023).
24. Matsukuma, K. E., Wei, D., Sun, K., Ramsamooj, R. & Chen, M. Diagnosis and differential diagnosis of hepatic graft versus host disease (GVHD). *J. Gastrointest. Oncol.* **7**, S21-31 (2016).
25. Qureshi, O. S. *et al.* Trans-endocytosis of CD80 and CD86: a molecular basis for the cell-extrinsic function of CTLA-4. *Science* **332**, 600–603 (2011).
26. Cambier, S., Gouwy, M. & Proost, P. The chemokines CXCL8 and CXCL12: molecular and functional properties, role in disease and efforts towards pharmacological intervention. *Cell. Mol. Immunol.* **20**, 217–251 (2023).
27. Tossetta, G., Piani, F., Borghi, C. & Marzioni, D. Role of CD93 in Health and Disease. *Cells* **12**, 1778 (2023).
28. Minguela, A. *et al.* CD28/CTLA-4 and CD80/CD86 costimulatory molecules are mainly involved in acceptance or rejection of human liver transplant. *Hum. Immunol.* **61**, 658–669 (2000).

29. Kennedy, A. *et al.* Differences in CD80 and CD86 transendocytosis reveal CD86 as a key target for CTLA-4 immune regulation. *Nat. Immunol.* **23**, 1365–1378 (2022).
30. Nierkens, S. *et al.* Differential requirement for CD28/CTLA-4-CD80/CD86 interactions in drug-induced type 1 and type 2 immune responses to trinitrophenyl-ovalbumin. *J. Immunol. Baltim. Md 1950* **175**, 3707–3714 (2005).
31. Shimizu, Y. *et al.* Dysregulated metabolic pathways of pulmonary fibrosis and the lipids associated with the effects of nintedanib therapy. *Respir. Res.* **26**, 166 (2025).
32. Çeker, G. *et al.* Effects of antifibrotic agent Nintedanib on experimentally generated priapism model in rats. *World J. Urol.* **43**, 619 (2025).
33. Ratajczak, M. Z., Serwin, K. & Schneider, G. Innate immunity derived factors as external modulators of the CXCL12-CXCR4 axis and their role in stem cell homing and mobilization. *Theranostics* **3**, 3–10 (2013).
34. Green, M. M. B. *et al.* Plerixafor (a CXCR4 antagonist) following myeloablative allogeneic hematopoietic stem cell transplantation enhances hematopoietic recovery. *J. Hematol. Oncol.J Hematol Oncol* **9**, 71 (2016).
35. Schroeder, A. *et al.* Scaling up spatial transcriptomics for large-sized tissues: uncovering cellular-level tissue architecture beyond conventional platforms with iSCALE. 2025.02.25.640190 Preprint at https://doi.org/10.1101/2025.02.25.640190 (2025).
36. Vasaturo, A. *et al.* Abstract 2075: Combining Vizgen's MERSCOPE spatial transcriptomics profiling and InSituPlex (ISP) multiplex immunofluorescence (mIF) to unravel the complexity of the tumor-immune microenvironment (TiME). *Cancer Res.* **85**, 2075–2075 (2025).

37. Fei, Y., Wu, Y., Chen, L., Yu, H. & Pan, L. Comprehensive pan-carcinoma analysis of ITGB1 distortion and its potential clinical significance for cancer immunity. *Discov. Oncol.* **15**, 47 (2024).
38. Xu, C., Xie, X.-L., Kang, N. & Jiang, H.-Q. Evaluation of ITGB1 expression as a predictor of the therapeutic effects of immune checkpoint inhibitors in gastric cancer. *BMC Gastroenterol.* **23**, 298 (2023).
39. Lin, E., Kuo, P.-H., Liu, Y.-L., Yang, A. C. & Tsai, S.-J. Transforming growth factor-β signaling pathway-associated genes SMAD2 and TGFBR2 are implicated in metabolic syndrome in a Taiwanese population. *Sci. Rep.* **7**, 13589 (2017).
40. Deng, Z. *et al.* TGF-β signaling in health, disease and therapeutics. *Signal Transduct. Target. Ther.* **9**, 61 (2024).
41. Ben Mousa, A. Sorafenib in the treatment of advanced hepatocellular carcinoma. *Saudi J. Gastroenterol. Off. J. Saudi Gastroenterol. Assoc.* **14**, 40–42 (2008).
42. Llovet, J. M. *et al.* Sorafenib in Advanced Hepatocellular Carcinoma. *N. Engl. J. Med.* **359**, 378–390 (2008).
43. Noronha, V. *et al.* Gefitinib vs Gefitinib Plus Pemetrexed and Carboplatin Chemotherapy in *EGFR* -Variant Lung Cancer—Long-Term Results of a Randomized Clinical Trial. *JAMA Oncol.* **10**, 824 (2024).
44. Sordella, R., Bell, D. W., Haber, D. A. & Settleman, J. Gefitinib-sensitizing EGFR mutations in lung cancer activate anti-apoptotic pathways. *Science* **305**, 1163–1167 (2004).

45. Zhong, W.-Z. *et al.* Gefitinib Versus Vinorelbine Plus Cisplatin as Adjuvant Treatment for Stage II-IIIA (N1-N2) EGFR-Mutant NSCLC: Final Overall Survival Analysis of CTONG1104 Phase III Trial. *J. Clin. Oncol.* **39**, 713–722 (2021).
46. Oliveira, M. F. D. *et al.* High-definition spatial transcriptomic profiling of immune cell populations in colorectal cancer. *Nat. Genet.* **57**, 1512–1523 (2025).
47. Sui, X. *et al.* Scalable spatial single-cell transcriptomics and translatomics in 3D thick tissue blocks. *Nat. Methods* **22**, 2574–2584 (2025).

Figure Legends

Figure 1 The Workflow of SpaTiAl Receptor-Ligand Analysis for Cell-Cell Communication (STARComm). | **a**, Conceptual framework: cell–cell communication is inferred based on spatial proximity, where ligand-expressing (sender) cells are more likely to interact with nearby receptor-expressing (receiver) cells. **b**, Tissue samples are collected and processed using spatial transcriptomics (e.g., Xenium). **c**, Ligand–receptor pairs are curated from public databases (e.g., CellChat, CellPhoneDB, SpaTalk) or custom lists (top) and matched to the genes measured in the spatial transcriptomics data (bottom). **d**, In situ maps of four ligand–receptor pairs (C1QA–CD93, CCL5–SDC4, CDH1–EGFR and CD86–CTLA4) and their overlay at a tertiary lymphoid structure (right), illustrating a multicellular communication interaction module (MCIM): a set of co-localized ligand–receptor interactions. **e**, Spatial transcriptomics data with annotated cell types visualized by color. **f**, Communication edges are inferred by identifying ligand-expressing and receptor-expressing cells using TACIT and then connecting cells within a 50μm spatial radius. **g**, The tissue is partitioned into spatial bins; ligand-receptor edges are counted per bin. **h**, Kernel density estimation generates a spatial map of communication density for each ligand-receptor pair. **i**, Communication densities are summarized in a matrix (bins × ligand-receptor pairs), where values represent interaction densities. **j**, This matrix is clustered (Leiden) to identify MCIMs, shown in UMAP space (top) and mapped back to the tissue (bottom). **k**, Heatmap of communication densities for each MCIM. **l**, MCIMs are grouped by signaling pathway and mapped onto spatial tissue architecture. **m–n**, MCIMs can be associated with clinical outcomes (m; illustrative Kaplan–Meier comparison by MCIM-3 abundance, log-rank P = 0.031) and linked to drug–target annotations with spatial Drug2Cell (n), as hypothesis-generating downstream analyses.

Figure 2. Benchmarking STARComm on a human GVHD salivary gland region profiled by Xenium. a, Spatial map of annotated cell types across a representative GVHD minor salivary

gland region profiled by Xenium spatial transcriptomics. Cell types were annotated using TACIT and include B cells, capillaries, $CD4^+$ T cells, $CD8^+$ exhausted T cells, dendritic cells, ductal cells, ductal progenitors, fibroblast progenitors, fibroblasts, IgA plasma cells, mucous acinar cells, and seromucosal acinar cells. **b,** Cluster assignments from STARComm, COMMOT, and SpatialDM overlaid on the same tissue section. STARComm produces spatially localized, anatomically coherent clusters, whereas COMMOT and SpatialDM yield diffuse assignments spanning the tissue. **c, Left**: Moran's I per cluster for each method. STARComm clusters show significantly greater above-chance spatial concentration than both COMMOT and SpatialDM. **Right**: observed versus permutation-expected Moran's I per cluster, with point size proportional to cluster cell count. Points above the diagonal indicate spatial concentration exceeding chance; COMMOT and SpatialDM clusters fall near the diagonal, reflecting inflation by large, tissue-spanning assignments. **d,** Percentage of canonical TLS-associated immune cells (B cells, $CD4^+$ T cells, $CD8^+$ exhausted T cells, dendritic cells, and IgA plasma cells) within each method's top-enriched cluster. STARComm Cluster 0 captures 34.9% of TLS immune cells, compared to 19.2% for SpatialDM and 20.8% for COMMOT. **e,** Computational runtime comparison. STARComm completes the analysis in ~5 minutes, compared to ~24 hours for SpatialDM and ~36 hours for COMMOT, representing an approximately 300-fold reduction in runtime.

Figure 3: STARComm identifies recurrent communication modules across GVHD salivary gland tissues | a, Overview of chronic GVHD manifestations across organ systems in the patient cohort. Percentages indicate the frequency of organ involvement across individuals. **b**, Cohort composition showing 35 samples collected from 23 patients, including both healthy controls and GVHD cases. **c**, Spatial transcriptomics was performed using the Xenium platform on minor salivary gland tissue microarrays (TMAs), enabling single-cell resolution mapping of gene expression. **d**, Integration of ligand-receptor spatial networks across tissues identified MCIMs based on recurrent cellular interaction patterns (top). These MCIMs were annotated using KEGG

and GO enrichment and evaluated for therapeutic relevance using the newly developed spatial Drug2Cell pipeline (bottom). **e–f**, UMAP visualization of bin-level communication densities across all tissues, colored by patient ID (e) and MCIM membership (f). **g**, Heatmap showing ligand-receptor density within each MCIM, highlighting signaling pathways associated with disease. **h**, Proportion plot illustrating the distribution of specific MCIMs across 35 tissue samples. **i**, Heatmap depicting enrichment scores of sender::receiver cell-type pairs within each MCIM.

Figure 4: Disease-associated MCIMs distinguish GVHD from healthy salivary gland tissue. | **a**, Visualization of cell type composition in representative healthy and GVHD minor salivary gland samples. Periductal inflammation resembling tertiary lymphoid structures (TLS) is highlighted in the inset. **b**, Spatial maps of four ligand-receptor pairs (CD86–CTLA4, CCL5–SDC4, CD274–CD80, and CDH1–EGFR) using a 50 μm proximity filter. The first three pairs show strong colocalization within TLS regions, while CDH1–EGFR is enriched in healthy tissues but absent from TLS regions. **c**, Ligand-receptor communication density maps highlight spatially enriched zones of signaling activity. **d**, MCIMs identified across individual samples reveal heterogeneous communication profiles within GVHD-affected tissues. **e**, Bar plot showing the distribution of MCIMs in healthy versus GVHD tissues, illustrating disease-associated shifts in multicellular communication. **f**, Principal component analysis (PCA) of MCIM proportions distinguishes healthy and GVHD tissues based on communication profiles. **g**, Boxplot of overall communication density per tissue area shows higher crosstalk in GVHD tissues. **h**, Boxplot comparing the proportions of individual MCIMs between healthy and GVHD tissues, MCIM-0 and MCIM-2 are higher in GVHD and MCIM-6 is higher in healthy tissues. **i**, Boxplots comparing of individual ligand–receptor pairs between GVHD and healthy tissues.

Figure 5: STARComm identifies conserved and tumor-specific communication programs across cancer types |. **a**, The spatial maps display each cancer type with regions colored

according to their associated MCIMs, highlighting distinct communication modules within the tissue. **b**, The UMAP visualization shows the density of spatial regions, with the top plot coloring regions by cancer origin and the bottom plot by MCIMs, revealing clear clustering patterns that differentiate tissue types and interaction networks. **c**, The bar plot quantifies the proportions of each MCIM across 16 tissue regions and eight cancer types, demonstrating variability in cell–cell communication patterns. **d**, The accompanying bar chart indicates the number of patients in which each MCIM accounts for more than 5% of tissue regions, emphasizing the prevalence of specific modules. **e**, Spatial maps of tumor regions highlight key ligand-receptor (R–L) interactions, TGFB1–ENG in melanoma (mapped to bintrafusp alfa) and TGFB1–TGFBR3 in prostate cancer (mapped to vactosertib), overlaid on tumor cells. **f**, KEGG pathway enrichment of MCIM ligand–receptor genes (dot size, rich factor; color, −log10 P). **g**, The dot-heatmap presents MCIMs (columns) and ligand–receptor pairs (rows) with the drug mapped to each pair by spatial Drug2Cell (right); dot size, percentage of bins expressing; color, average expression. Highlighted pairs are shown in e. Mappings are hypothesis-generating.

Figure 6: Benchmarking and application of STARComm to intra-tumoral communication heterogeneity in uterine cancer | a, shows the spatial map highlighting different cell populations within the tissue, and a small ROI. **b**, Comparison of spatial cell–cell communication patterns generated using STARComm, COMMOT, and SpatialDM. **c**, Heatmap of the top ligand–receptor pairs distinguishing the two STARComm region-of-interest clusters. **d**, Moran's I of cluster assignments for the three methods (STARComm 0.91, COMMOT 0.19, SpatialDM 0.13). **e**, Runtime for the ~6,000-cell region (STARComm 2 min, SpatialDM 25 min, COMMOT 19 h 35 min). **f**, Spatial distribution of MCIMs across the entire tissue, depicting three distinct regions characterized by unique patterns of cell–cell co-location and communication; accompanying density maps show WNT5A–FZD7, ICAM1–MUC1 and CEACAM1–EGFR. **g**, Heatmap of ligand–receptor communication density across bins of MCIMs 16, 1 and 3. **h**, Enrichment of

sender::receiver cell-type pairs within MCIMs 16, 1 and 3. Finally, **i**, GO biological process enrichment for MCIMs 1, 3 and 16 (color, −log10 adjusted P).

Figure 7: **STARComm resolves multicellular communication modules in 3D spatial transcriptomic and translatomic data | a**, 3D visualization of the spatial distribution of diverse cell types—including various excitatory and inhibitory neurons, astrocytes, and oligodendrocytes—annotated within the 150-μm thick DeepSTARmap (transcriptome) and DeepRIBOmap (translatome) tissue blocks. **b**, 3D mapping of the nine distinct Multicellular Communication Interaction Modules (MCIMs) identified by STARComm, illustrating spatially organized signaling hubs across the mouse brain. **c**, (Left) Overall communication density in the transcriptome (6.47×10^{-6}) and translatome (5.07×10^{-6}). (Right) Venn diagram showing the overlap of communication signals, with 198 interactions (91%) shared between layers and 20 interactions (9%) unique to the transcriptome. **d**, Interaction scores of 218 ligand–receptor pairs in Deep-RIBOmap (translatome, x-axis) versus Deep-STARmap (transcriptome, y-axis); Pearson r = 0.64. **e**, To evaluate the impact of spatial dimensionality on cellular interactomes, we compared 3D MCIM distributions (left) with virtual 5-μm sections along the z-axis (right). The bar plot shows total communication events detected in the 3D volume (90,583) and summed across virtual 2D sections (6,311).

Table 1. Comparison of cell–cell communication inference tools for single-cell RNA-seq and spatial transcriptomics data. Tools are organized into three categories: (i) scRNA-seq ligand–receptor methods that operate on expression-space graphs without spatial coordinate input; (ii) spatial CCC methods that require cell-type annotation as input; and (iii) spatial CCC methods that are annotation-free and model communication directly from native spatial coordinates (green-shaded rows). The annotation-free spatial group defines the benchmark comparator set for STARComm. Within each category, tools are ordered chronologically by

publication date. Input data types are specified as scRNA-seq (dissociated), Spot (spot-based platforms, e.g. Visium, ST), or SC spatial (single-cell resolution platforms, e.g. MERSCOPE, Xenium, CosMx). 3D support indicates native compatibility with 3D spatial transcriptomics data. Scalability is reported as approximate throughput (cells or spots/min); entries marked (GPU) requires GPU acceleration. Scalability is approximate for datasets of ~5–10k cells; actual usage varies with dataset size and hardware.

Supplementary Figure Legends

Supplementary Figure 1: Simulation benchmark of module recovery. a, Simulated tissue (3,000 cells) with four ground-truth MCIMs, each defined by a unique set of ligand–receptor interactions. b, Representative maps of each simulated MCIM with receptor and ligand expression. c, Left: Negative Binomial expression distributions for background ($\mu = 2$) and communicating cells ($\mu =$ 6, 20 shown); middle: example expression maps at increasing μH; right: ARI versus μH (4–40) with 10 ligand–receptor pairs for STARComm, ExpressionOnly, COMMOT and SpatialDM. d, Left: example maps at 10%, 40% and 100% communication density (fraction of neighbouring cell pairs within 50 μm carrying communication); right: ARI versus communication density with $\mu H = 6$ and 50 ligand–receptor pairs. e, ARI of STARComm using different expression-binarization rules (non-zero, 20th/50th/90th percentile, mean + 2 SD, mean + 1 SD, Otsu, IQR fence and TACIT optimal). f, Runtime (seconds, log scale) of each method. g, Representative low-density simulation: ground truth and module assignments from each method. h, Moran's I of module assignments by method.

Supplementary Figure 2: Additional simulation benchmarks in 2D. a, ARI versus μH with 20 (left) and 100 (right) ligand–receptor pairs (n = 3,000 cells). b, ARI versus communication density with $\mu H = 10$ and 50 ligand–receptor pairs. c, ARI versus μH with 50 ligand–receptor pairs. d, ARI by number of ligand–receptor pairs (10, 20, 50 and 100). e, STARComm ARI as a function of KDE bandwidth h (μm).

Supplementary Figure 3: a, UpSet plot of ligand–receptor communications shared between and unique to the eight cancer types. b, Communications unique to each cancer type. c, Density heatmap of ligand–receptor pairs across the 24 pan-cancer MCIMs.

Supplementary Figure 4: a, Spatial maps display four tissue regions, with MCIMs color-coded to distinguish two colon cancer areas (P2 CRC and P5 CRC) and two healthy regions (P3 NAT and P5 NAT). **b**, Communication per tissue area in cancer versus normal adjacent tissue. **c**, The volcano plot highlights differentially enriched ligand-receptor pairs between healthy and cancer regions, emphasizing specific signaling interactions associated with malignancy. **d**, The heatmap portrays signature R–L pairs characterizing each MCIM, revealing distinct communication profiles across regions. **e**, Proportion of each MCIM per section. **f**, with MCIM 6 (pink) notably enriched in tumor areas (red), suggesting its prominent role in tumor microenvironment interactions. **g**, Chord diagram of the cell types communicating within MCIM-6.

Tool	Input data type	3D support	Requires annot.	Spatial distance modeling	Methodology	Output level	Scalability (cells|spots/min)
scRNA-seq ligand–receptor tools							
CellPhoneDB 2020 · Nat Protoc	scRNA-seq	–	Yes	— *(expression space)*	**Statistical** Permutation test on L-R co-expression across cell types	**Population-level** Significant L-R pairs per cell-type pair	~2,000
NicheNet 2020 · Nat Methods	scRNA-seq	–	Yes	— *(expression space)*	**Statistical + ML** Prior-knowledge network + regression; ligand → targets	**Network** Prioritized ligands with downstream target links	~1,000
SingleCellSignalR 2020 · NAR	scRNA-seq	–	Yes	— *(expression space)*	**Statistical** Regularized product-based L-R score (LRscore)	**Population-level** Scored L-R pairs per cell-type pair	~5,000
NICHES 2022 · Brief Bioinform	scRNA-seq	–	**No**	— *(expression space)*	**Statistical** Pairwise cell–cell L-R product scoring on neighbor graph	**Cell-pair level** Per-edge L-R scores; not native spatial	~2,000
LIANA+ 2024 · Nat Cell Biol	scRNA-seq, Spot	–	Yes	— *(expression space)*	**Meta-framework** Consensus scoring across multiple CCC methods	**Population-level** Consensus-ranked L-R pairs	Varies
Spatial CCC tools — require cell-type annotation							
CellChat v2 2023 · Nat Commun	scRNA-seq, Spot	–	Yes	Hard distance cutoff (v2)	**Statistical** Mass action model + NMF patterns	**Population-level** Cell-type pair L-R + pathway patterns	~500
SpaTalk 2023 · Nat Commun	scRNA-seq + Spot	–	Yes	Spatial graph (distance-based edges)	**Deep learning** GNN on spatial cell-type graph + downstream targets	**Network** Cell-type pair L-R with target pathways	**~250 (GPU)**
stMLnet 2023 · Genome Res	Spot	–	Yes	Distance-weighted diffusion	**Stat. / mechanistic** Mass action + diffusion; LR→TF→target	**Network** Multilayer: L-R → TF → targets	~100
SpaCCC 2024 · Big Data Min Anal	Spot	–	Yes	LLM embedding similarity	**Deep learning** Fine-tuned scGPT + permutation test	**Population-level** L-R scores per cell-type pair	~100
TWCOM 2024 · Bioinform Adv	scRNA-seq, Spot	–	Yes	Tweedie regression on pairwise distance	**Statistical** Tweedie distribution / GAM	**Population-level** Distance-dependent L-R significance	~1,000
Spatial CCC tools — annotation-free, native spatial coordinates							
COMMOT 2023 · Nat Methods	Spot, SC spatial	–	**No**	Optimal transport with distance kernel	**Optimization + ML** Collective OT; L-R competition across space	**Cell-level** Per-cell directional signaling vectors	**~10 (GPU)**
SpatialDM 2023 · Nat Commun	Spot, SC spatial	–	**No**	Spatial autocorrelation (bivariate Moran's I)	**Statistical** Bivariate Moran's I; permutation test	**Cell-level** Global L-R significance + local hotspots	~40
CellNEST 2025 · Nat Methods	Spot, SC spatial	**Yes**	**No**	Graph attention on spatial k-NN	**Deep learning** GAT + contrastive learning	**Network** Multi-hop L-R→L-R relay chains	**~10 (GPU)**
STARComm	SC spatial	**Yes**	**No**	KDE density estimation + spatial binning	**Machine learning** Spatial density clustering (Leiden) on R-L activity	**Spatial modules** MCIMs: co-localized multi-R-L hubs	~1,000

Abbreviations: CCC, cell–cell communication; GAM, generalized additive model; GAT, graph attention network; GNN, graph neural network; KDE, kernel density estimation; L-R, ligand–receptor; MCIM, multicellular communication interaction module; NMF, non-negative matrix factorization; OT, optimal transport; SC, single-cell; ST, spatial transcriptomics; TF, transcription factor. Green-shaded rows indicate the annotation-free benchmark comparator group.

Figures

Figure 1

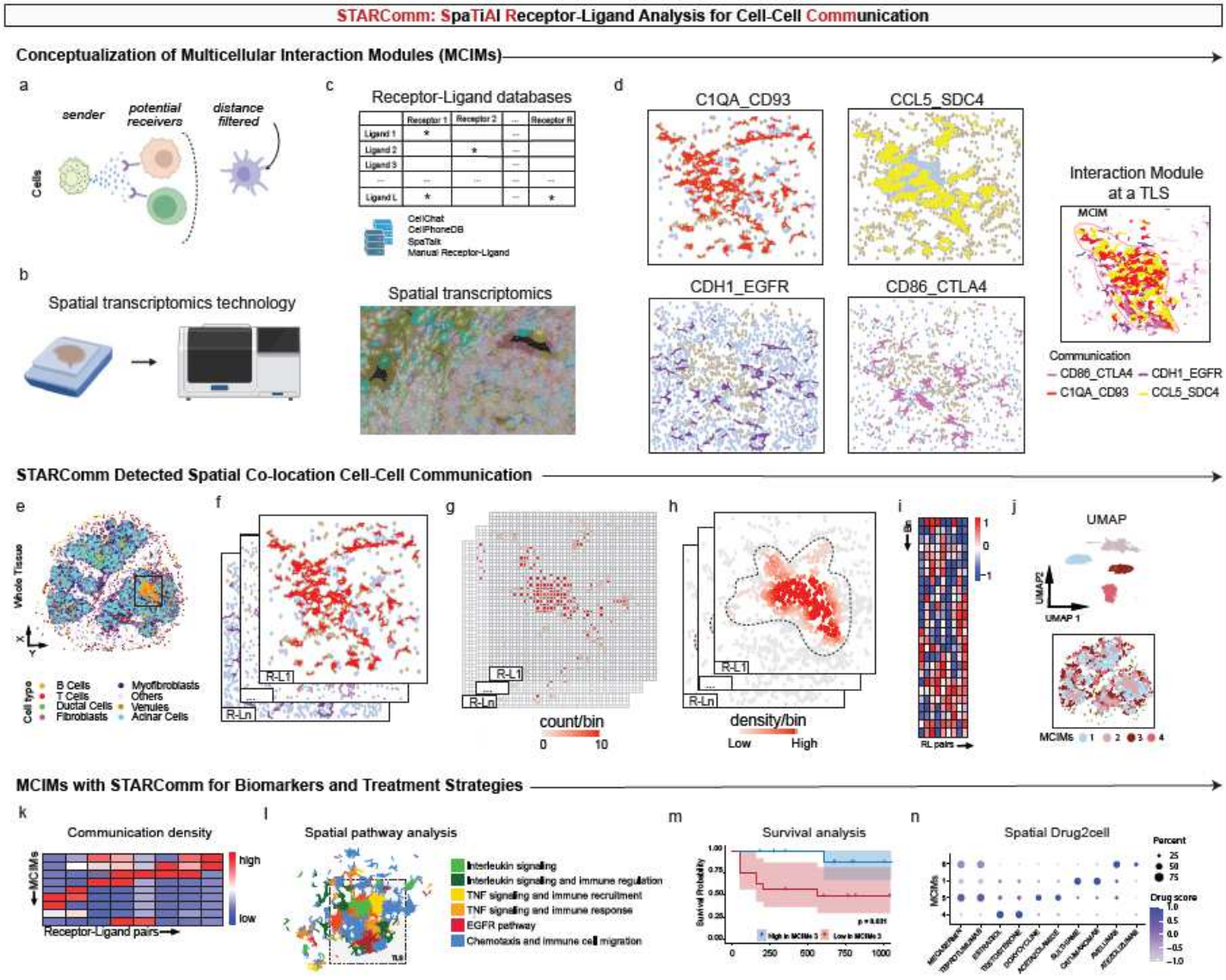

Figure 1

See image above for figure legend

Figure 2

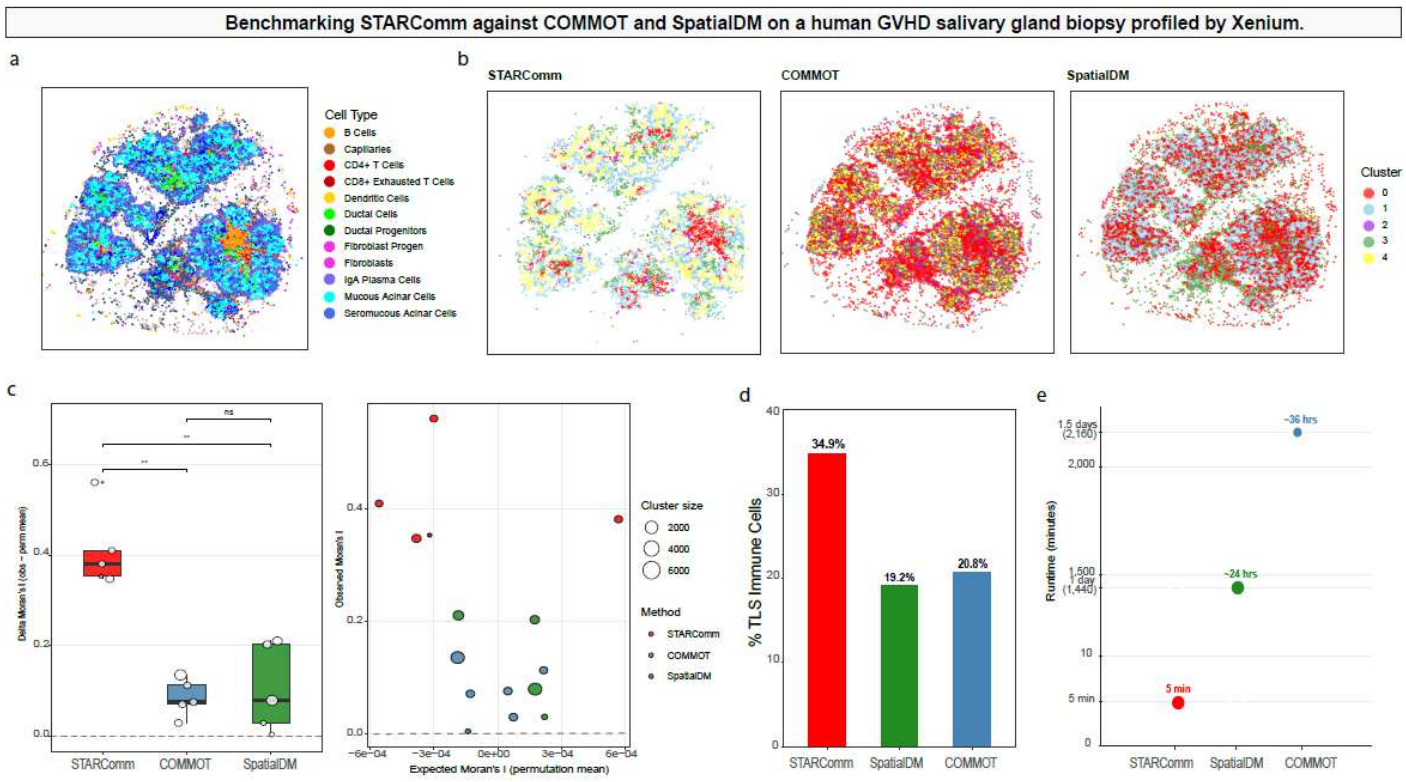

Figure 2

See image above for figure legend

Figure 3

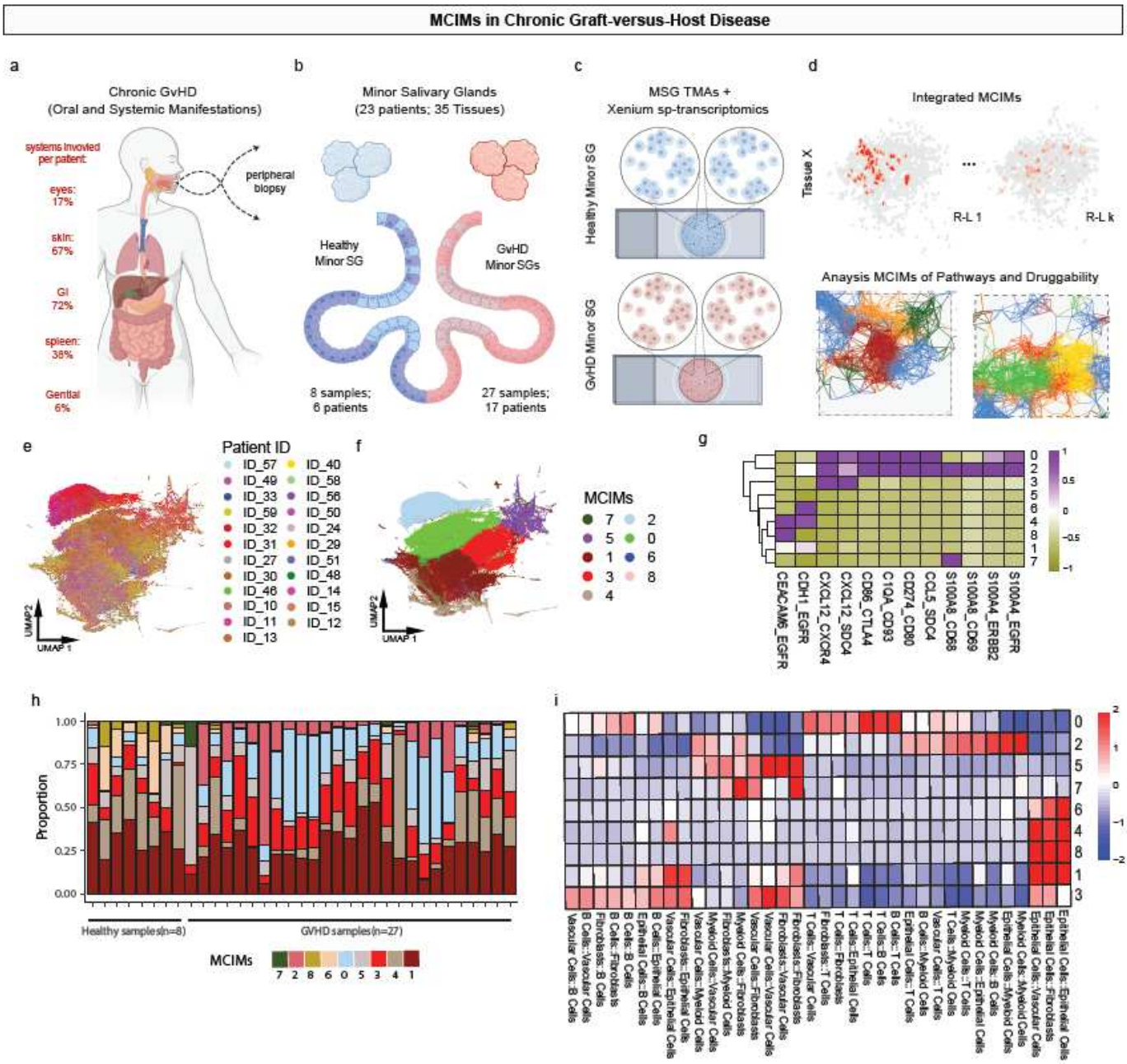

Figure 3

See image above for figure legend

Figure 4

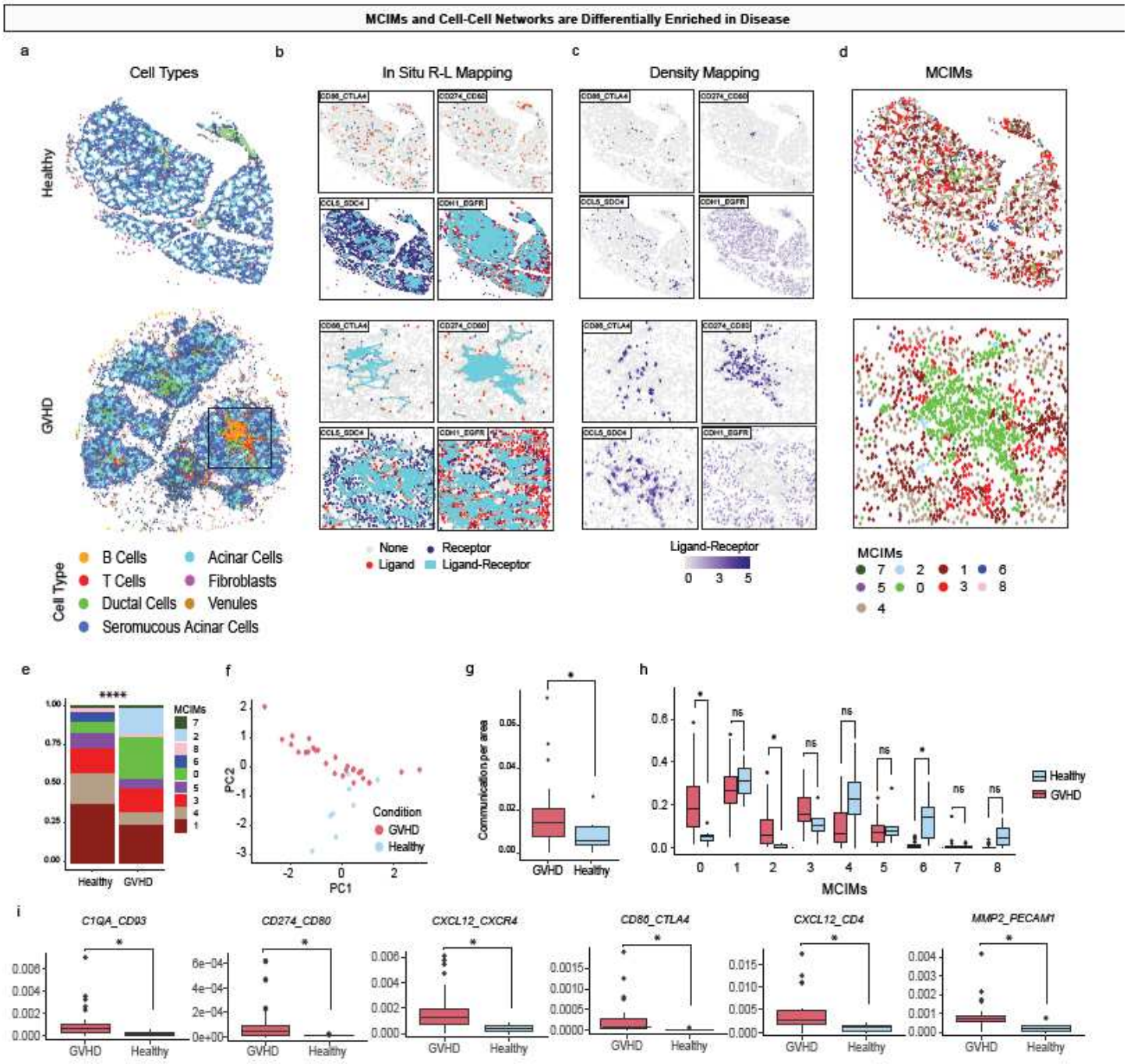

Figure 4

See image above for figure legend

Figure 5

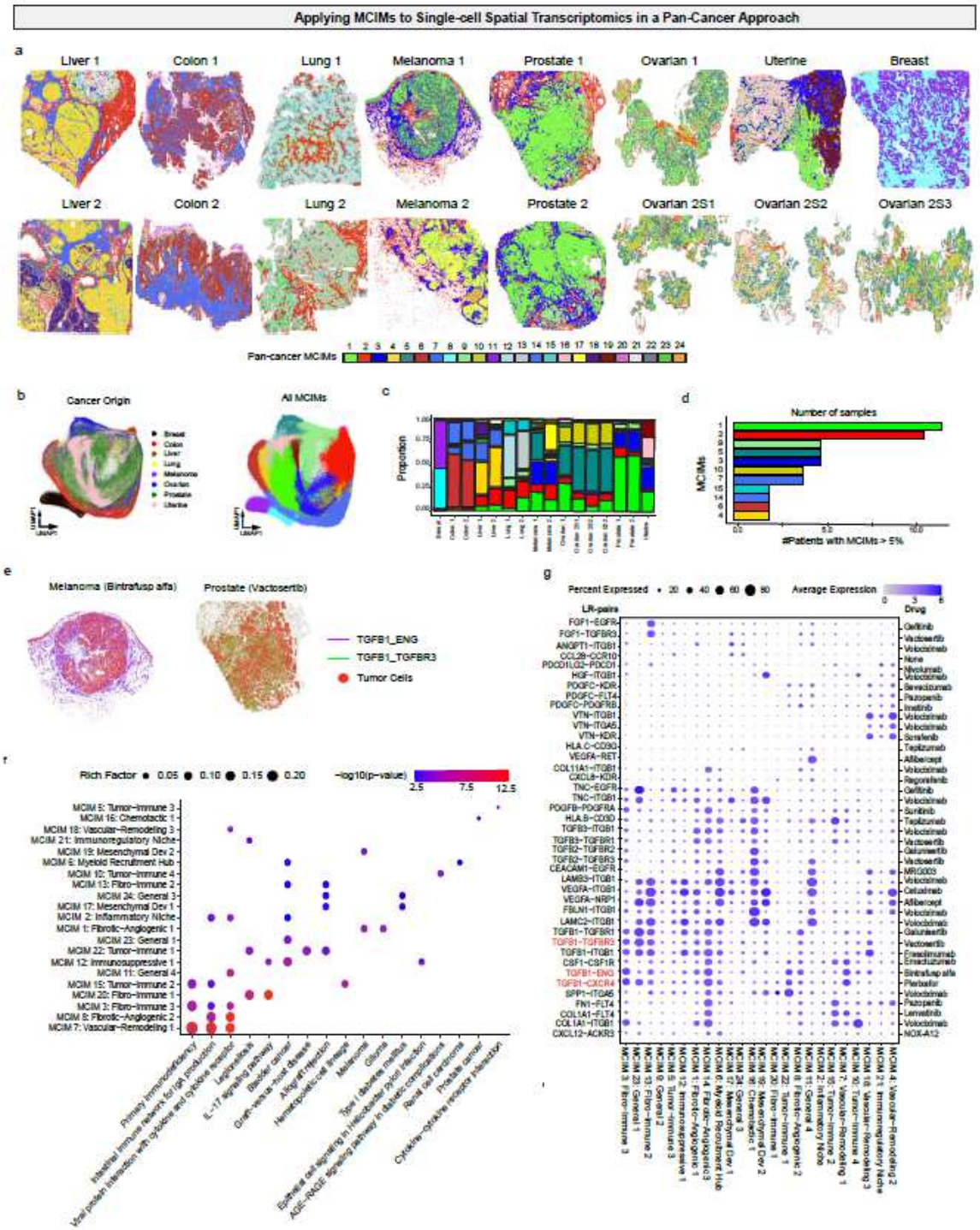

Figure 5

See image above for figure legend

Figure 6

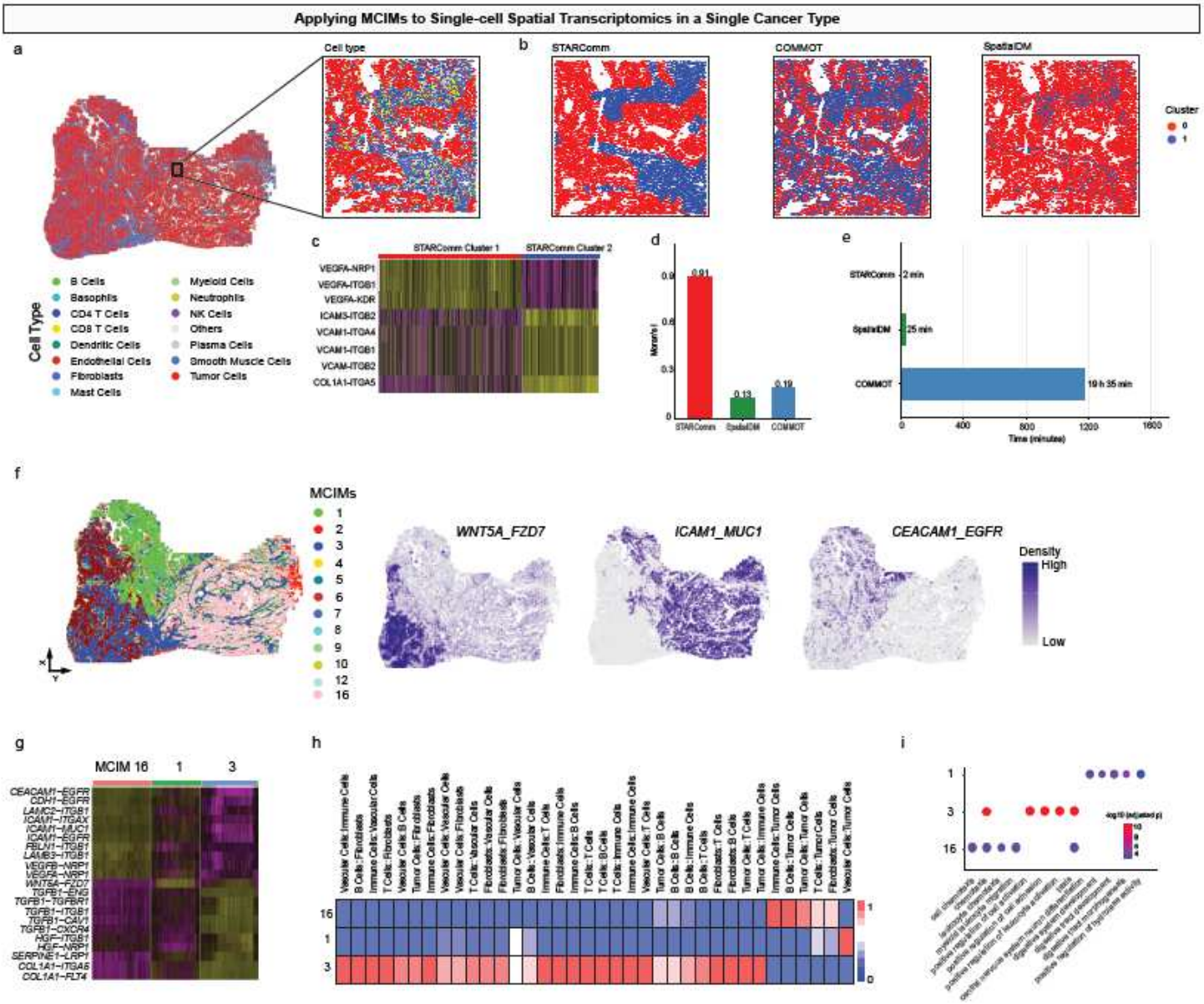

Figure 6

See image above for figure legend

Figure 7

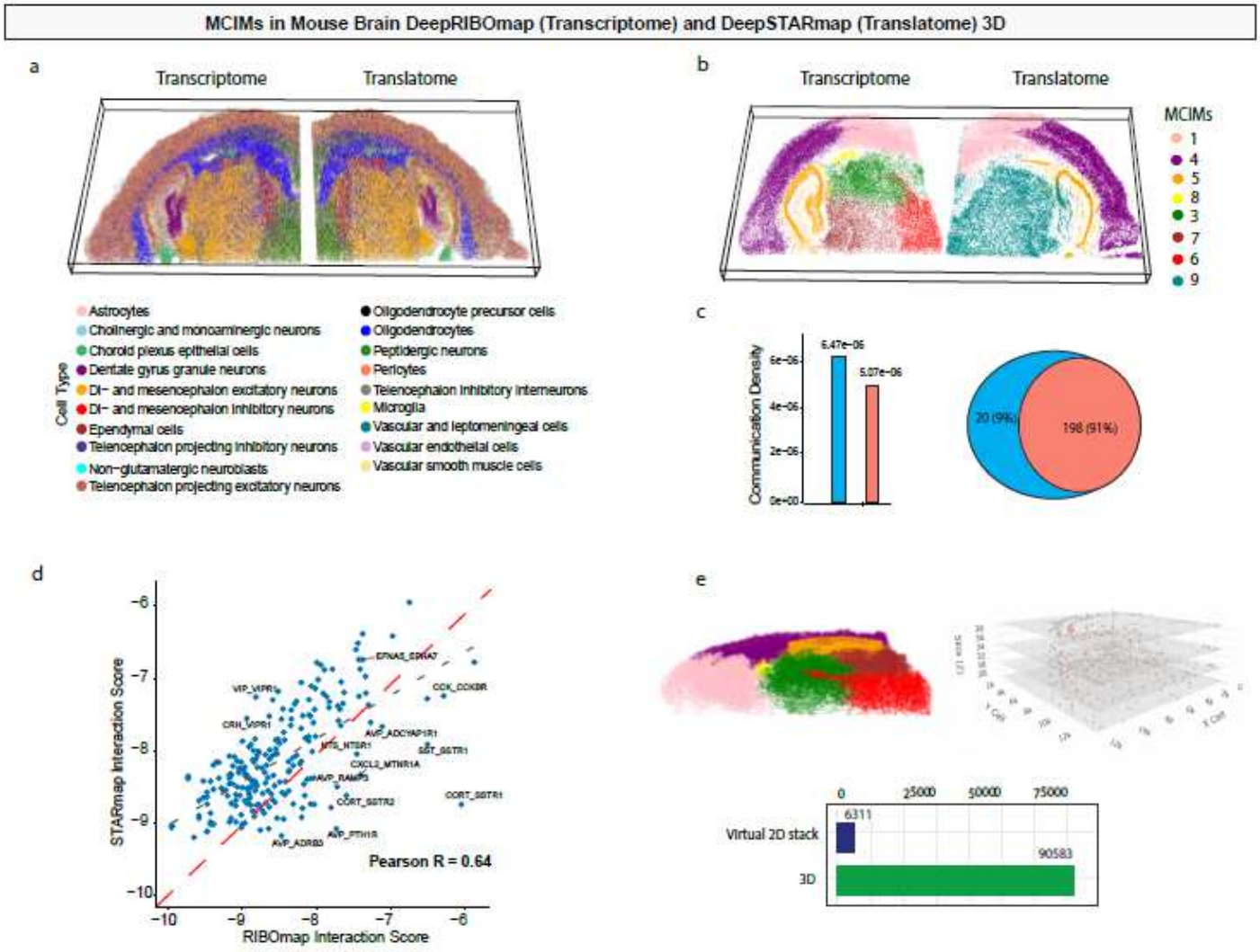

Figure 7

See image above for figure legend

Supplementary Files

This is a list of supplementary files associated with this preprint. Click to download.

- SupFigure1.pdf
- SupFigure2.pdf
- SupFigure3.pdf
- SupFigure4.pdf